MOFs-derived Cu3P@CoP p-n heterojunction for photocatalytic hydrogen evolution

Lijun Zhang[1], Xuqiang Hao[1], Zhiliang Jin[2], and Tiansheng Zhao[3]

[1]North Minzu University
[2]Affiliation not available
[3]Ningxia University

May 5, 2020

Abstract

In this study, we developed a novel in situ growth scheme to construct the Cu-MOFs@ZIF-9(Co) core-shell precursor material. The Cu-MOFs@ZIF-9(Co) core-shell precursor was treated by low-temperature phosphorization to obtain a Cu3P@CoP composite catalyst with a self-supporting structure. Cu3P@CoP composite catalyst not only has a hierarchical structure, but also builds a p-n heterojunction at the interface. The unique structure and composition of Cu3P@CoP can promote charge migration and provide large surface area and rich active sites to drive water photolysis. In addition, by controlling the degree of phosphation of Cu-MOFs@ZIF-9(Co) material and adjusting the ratio of Cu and Co, it was found that the maximum hydrogen-producing activity of the composite photocatalyst reaches 469.95 μmol, and it has a very excellent cycle stability. The results of photoelectrochemical and fluorescence tests showed that the proper conduction and valence band of Cu3P and CoP formed a more effective path way for charge transfer.

1. Introduction

Facing the excessive use of fossil energy and the increasingly serious environmental pollution problem, the use of infinite solar energy is a possible and promising solution [1, 2]. Since Fujishima and Honda's research on the photoelectrochemical hydrogen production of titanium dioxide (TiO_2) photoanode in 1972, semiconductor-based photocatalysts have received widespread attention worldwide [3]. And many photocatalysts have been developed, such as TiO_2[4], CdS [5, 6], $Zn_{0.5}Cd_{0.5}S$ [7, 8], $BiVO_4$ [9], g-C_3N_4 [10, 11], MOFs and their derivatives [12]. However, the light conversion efficiency and photocatalytic performance have not improved significantly. In order to synthesize advanced high-efficiency photocatalytic materials, the research interest of semiconductor materials based on MOFs and its derivatives is increasing.

As an kind of emerging material, metal organic frameworks (MOFs) are important and potential materials in heterogeneous catalytic reactions due to its rich pore structure, large specific surface, high structural diversity, adjustable chemical properties, and highly dispersed metal sites [13, 14]. MOFs are used as precursors for the synthesis of MOF-based hybrid structures, which will provide more opportunities for the comprehensive conversion and application of MOFs and develop more unique potentials about MOFs. Low-temperature phosphating of different kinds of MOFs can lead to excellent performance of transition metal phosphides, such as Ni_2P [15, 16], CoP [17], FeP [18, 19] and NiCoP [20]. These phosphides, as n-type semiconductors, are favorable for accepting photo-generated electrons. In previous research reports, transition metal phosphides were mainly used as co-catalysts to enhance the photocatalytic H_2release to improve the separation and transport efficiency of electron-hole pairs [21, 22, 23]. In fact, the transition metal phosphide alone exhibits better photocatalytic performance under dye sensitization conditions, mainly due to its narrow band gap structure and strong light absorption capacity [24, 25].

A promising approach to enhance the catalytic performance of MOFs and their derivatives is to change MOFs into a core-shell structure [26]. Here, we have developed a novel in-situ growth scheme that combines the advantages of ZIF-9 and $Cu_3(BTC)_2$, and uses Cu-MOFs@ZIF-9(Co) core-shell material as a precursor to derive Cu_3P@CoP composite catalyst. Since Cu_3P is a p-type semiconductor and CoP is a n-type semiconductor, the Cu_3P@CoP composite catalyst obtained from Cu-MOFs@ZIF-9(Co) core-shell material not only has a layered structure, but also builds a p-n heterogeneity at the interface. In order to understand this phosphation more deeply, we control the degree of phosphation of Cu-MOFs@ZIF-9(Co) material on the one hand, and adjust the ratio of Cu to Co by changing the content of Cu-MOFs to explore its reasons and rules for the formation of photocatalytic activity. The unique structure and composition of Cu_3P@CoP can promote charge separation and migration, provide large surface area and rich active sites to drive water photolysis. The results show that the optimized Cu-Co-2P-2 photocatalyst exhibits generation activity of 469.95 μmol H_2 and has high stability. Our work will provide a new strategy for the rational design of efficient catalysts for MOFs derivatives.

2. Experimental

2.1. Cu-MOFs (Cu_3BTC_2) and ZIF-9(Co) preparation

In a typical synthesis process, 0.01 mmol Cu $(NO_3)_2{\cdot}3H_2O$ and 0.03 mmol 1,3,5 pyromellitic acid were firstly weighed and dissolved in 50 mL ethanol,then the mixture was stirred for 1 h and transferred to an oven at 140 °C for 24 h. After being washed and dried,blue Cu-MOFs powder was obtained. The synthesis of pure ZIF-9 was carried out in aqueous solution at room temperature. 0.23 g benzimidazole and 0.28 g Co $(NO_3)_3{\cdot}6H_2O$ were weighand dissolved in 40 ml of water.After the mixture was stirred for 15 min, it was added 5 mL of ammonia and then stirred for 45 min. Finally, it was kept in the dark for 8 h and dried by centrifuge to obtain the product.

2.2 Composite sample preparation

In the process of synthesizing ZIF-9, a certain amount of pre-synthesized Cu-MOFs was added during the aging process under dark conditions. Cu-Co-x(x = 1, 2, 3, 4. x refers to the changed Cu-MOFs mass) was obtained by adjusting the precursor of ZIF-9 synthesized by benzimidazole and $Co(NO)_3{\cdot}6H_2O$. Cu-Co-xP-2(x = 1, 2, 3, 4; x is the mass ratio of precursor to sodium hypophosphite) composite catalyst was obtained by phosphating different Cu-Co-2 (Cu-MOFs@ZIF-9) with a 0.125 g Cu-MOFs. Phosphating experiments of the catalyst were carried out under the conditions of nitrogen protection by calcination at 300 °C for 2 h. In addition, Cu-Co-x (x = 1, 2, 3, 4.) was subjected to phosphatization experiments of the same degree (sodium hypophosphite has twice the mass of Cu-Co-x) to obtain Cu-Co-2P-x (x = 1, 2, 3, 4.) composite catalyst. The phosphorylated products of pure Cu-MOFs and ZIF-9 are referred to as Cu-P and Co-P. The specific catalyst synthesis diagram is shown in Figure 1.

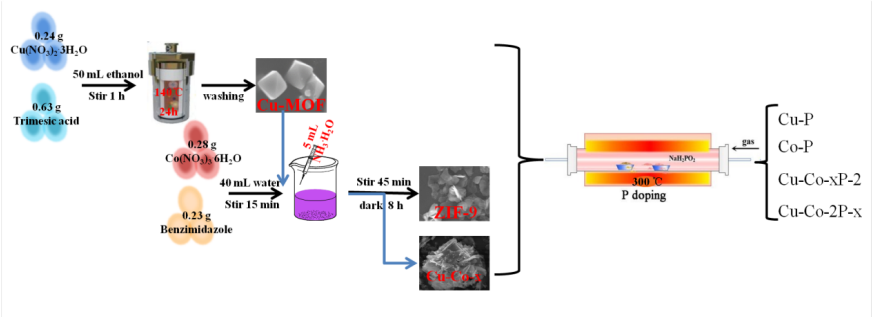

Figure 1. Schematic diagram of preparation of photocatalyst.

2.3 Characterization

X-ray Diffraction measurement of the obtained samples was carried out by an advanced diffractometer operating (HORIBA Scientific, France; 40 kV and 30 mA). SEM (Zeiss evo10) were used to obtain the morphology information about the samples. TEM: FEI Tecnai TF20 high-resolution transmission electron microscope. XPS testing was performed on an energy dispersive X-ray instrument (ESCALAB 250Xi) using energy dispersive X-ray analysis. UV-vis diffuse reflectance spectra were tested on a PerkinElmer Lambda-750 UV-vis-near-IRvia spectrometer using $BaSO_4$ as a reference for baseline correction. The N_2 adsorption-desorption isotherm of the sample was obtained at 77K using ASAP2020M. The PL spectrum were acquired by a FLUOROMAX-4 spectrophotometer at room temperature. Na_2SO_4 (0.2 M) aqueous solution was used as supporting electrolyte. In a standard three-electrode cell, the photoelectrochemical measurement was performed on an electrochemical analyzer (VersaStat4-400, Advanced measurement Technology, Inc).

2.4 Hydrogen production experiments

The tests of photocatalytic H_2 evolution performance were carried out in a 62 mL quartz reaction flask with a flat window. Specific steps were as follows: TEOA was used as the electron donor, photocatalyst powder and EY was added into TEOA aqueous solution (15%). Before light source irradiation, ultrasonic dispersion was used and lasted to form homogeneous solution, and nitrogen was used to replace the system air to form anaerobic environment. The photocatalyst in suspension was evenly dispersed with a magnetic stirrer. A 5 W LED white-light multi-channel was used as simulated solar light source in the photocatalytic reaction system. Each time 0.5 mL of evolved gas was extracted from the reaction flask to analyze the produced hydrogen amount by taking gas chromatography (Tianmei GC7900, TCD, 13Xcolumn, N_2 as carrier).

3. Results and discussion

3. 1

Morphology, structure and compositions analysis

The XRD patterns of the synthesized Cu-MOFs and ZIF-9(Co) are shown in Figure S1(a, b), which are consistent with the results reported in the literature [27, 28, 29]. After Cu-MOF and Co-MOFs are respectively phosphated, Cu-P and Co-P samples can be obtained. After fully phosphating ZIF-9,there exist typical diffraction peaks in 2ϑ = 31.60º, 35.18º, 36.34º, 46.19º, 48.18º, and 56.27º, as shown in Figure 2(a). The analysis can be indexed to the JCPDS#65-1474 standard card of CoP. The corresponding crystal planes are (011), (200), (111), (112), (211), and (202). The weakening of the intensity of all the peaks of CoP indicates relatively low degree of crystallization [30]. In the XRD pattern of Cu-P (Figure 2(b)), the corresponding characteristic peaks of Cu_3P (JCPDS#74-1067) and Cu element (JCPDS#70-3038) can be corresponded. The characteristic peaks of Cu_3P appear at 28.43º, 35.86º, 38.90º, 41.38º, 44.91º, 46.02º, 47.08º, 53.30º, 56.74º, 58.14º, 66.34º and 73.01°, corresponding to (111), (112), (022), (211), (300), (113), (122), (104), (311), (222), (223), and (322) crystal planes. The obvious diffraction peaks of (111) and (200) plane diffraction of elemental Cu are located at 43.17° and 50.29°. Figure 2(c) shows the results of Cu-Co-xP-2 (x = 1, 2, 3, 4.) composite catalysts obtained by phosphating at different degrees. The outer layer of ZIF-9 was gradually phosphorylated to produce diffraction peaks related to CoP. With the increasing of phosphating degree in the composite samples, the content of phosphide (Cu_3P, CoP) gradually increases, and the intensity of the related diffraction peaks gradually increases. Because the crystallinity of the outer phosphide is relatively low, the related diffraction peaks of the internal unphosphorized Cu-MOFs is enhanced. The spectrums of Cu-Co-x (x = 1, 2, 3, 4) obtained by adjusting the mass of nucleated Cu-MOFs and maintaining the quality of the outer layer ZIF-9 are shown in Figure S1(c). There are both Cu-MOFs and ZIF-9 peaks, and the diffraction peaks related to Cu-MOFs increase as the mass of Cu-MOFs increases. Cu-Co-x (x = 1, 2, 3, 4) was phosphorylated to obtain Cu-Co-2P-x (x = 1, 2, 3, 4.) composite catalyst (Figure 2(d)). With the increasing of the mass of Cu-MOFs under the same phosphatization degree, the diffraction peaks related to Cu-MOFs gradually decrease. Therefore, the Cu-Co-2P-4 sample only contains the diffraction peaks of Cu_3P, Cu and CoP, and there are no peaks of MOFs.

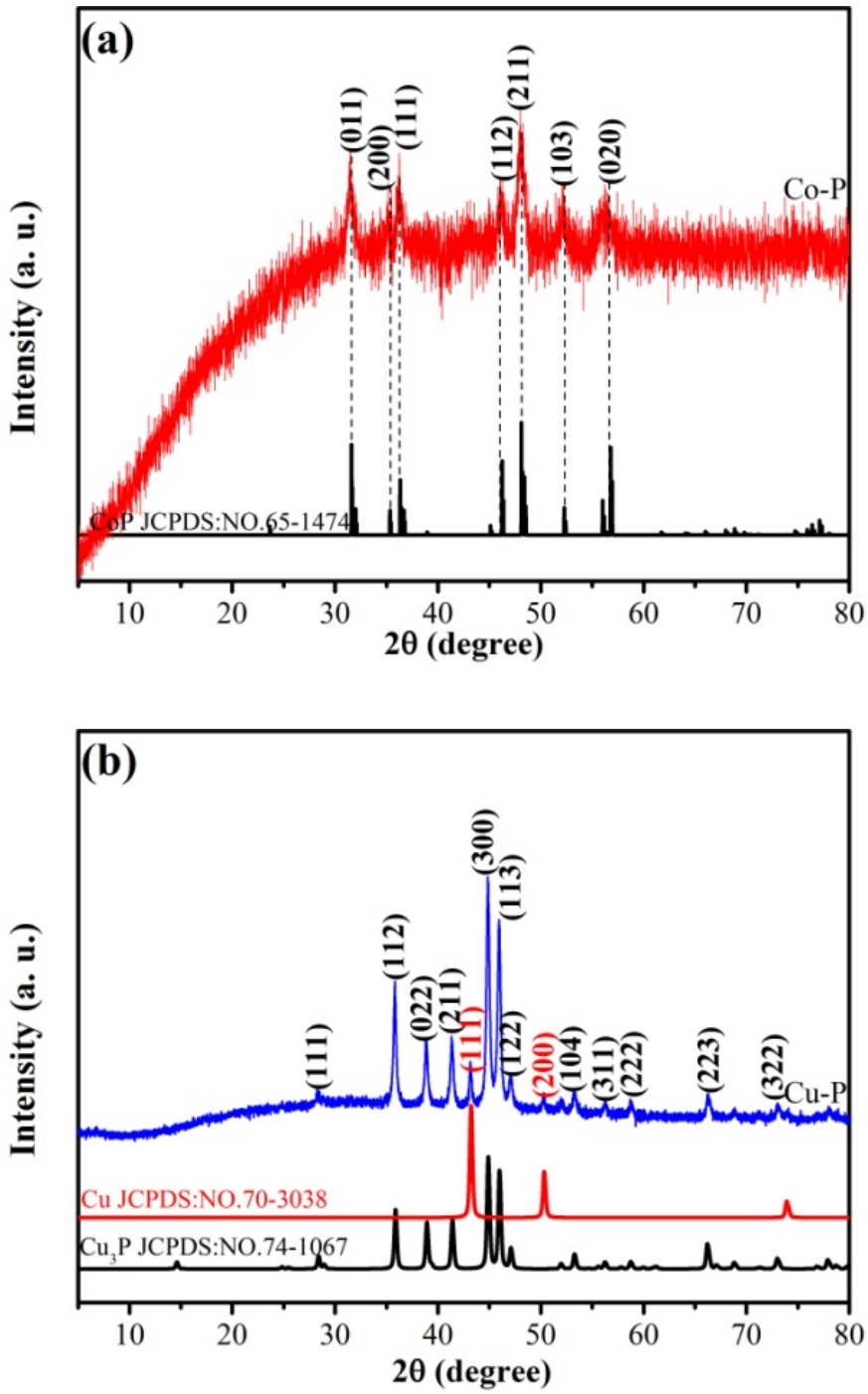

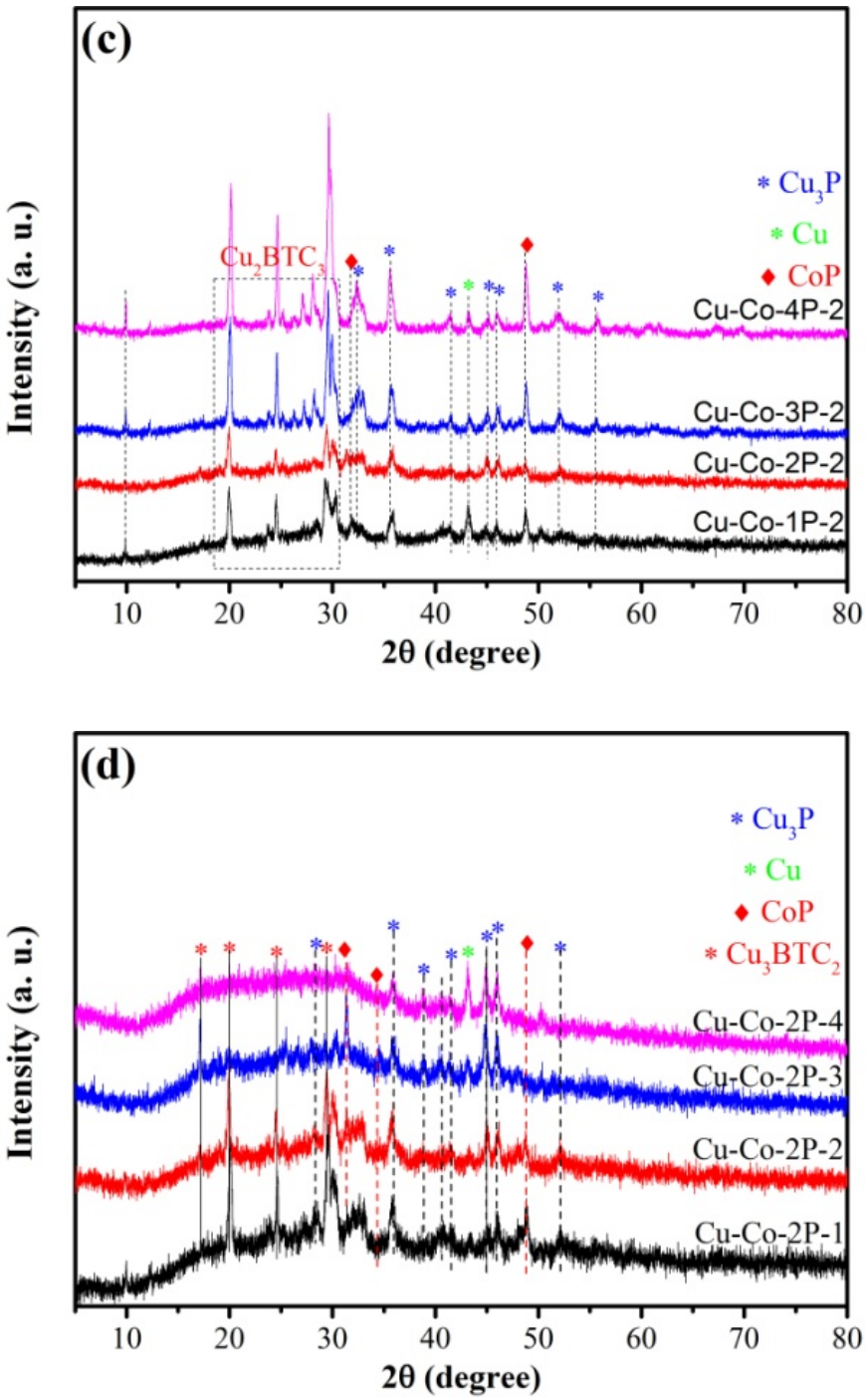

Figure 2. XRD patterns of Co-P (a); Cu-P (b); Cu-Co-xP-2(x= 1, 2, 3, 4.) (c); Cu-Co-2P-x(x= 1, 2, 3, 4.) (d).

The SEM images are shown in Figure 3, displaying the morphology characteristics of Cu-MOFs, ZIF-9(Co) and Cu-MOFs@ZIF-9(Cu-Co-2) as well as the samples after phosphating. In Figure 3(a), the sample of Cu-MOFs exists as a regular octahedron, and the surface is relatively flat. ZIF-9(Co) displays the morphology of the 2D nanosheet which is well-shaped and has averaged size (Figure 3(b)). When ZIF-9(Co) grows on the

surface of Cu-MOFs, the growth of 2D nanosheets is suppressed to a certain degree. Therefore, ZIF-9(Co) on the surface of Cu-MOFs in the Cu-Co-2 composite sample shown in Figure 3(c) exists in the form of fibrous rods or small pieces. Cu-P, Co-P and Cu-Co-2P-2 composite samples were obtained by phosphating Cu-MOFs, ZIF-9(Co) and Cu-Co-2 samples, as shown in Figure 3(d-f). Cu-P samples almost do not have regular geometric shapes, showing larger particles and more denser. The SEM image of Co-P obtained from the phosphorization of Co-MOFs of 2D nanosheets is shown in Figure 3(e). In Figure 3(e), Co-P shows a very uniform and fine flaky structure. The SEM image of Cu-Co-2P-2 sample obtained by phosphating the Cu-MOFs@ZIF-9(Cu-Co-2) sample is shown in Figure 3(f). In the composite sample, the surface of Co-MOFs is almost completely phosphatized, showing a small plate shape, and Cu-MOFs inside still have a small number of regular three-dimensional structures. Combined with XRD analysis, it can be seen that the phosphorization of Cu-MOFs is not complete, so there will be a small number of regular octahedral structures in Figure 3(f).

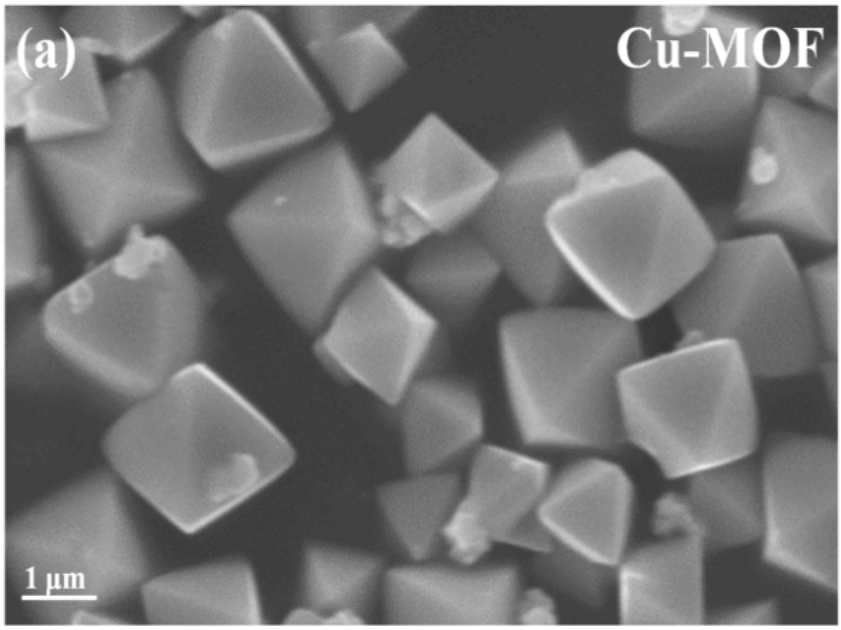

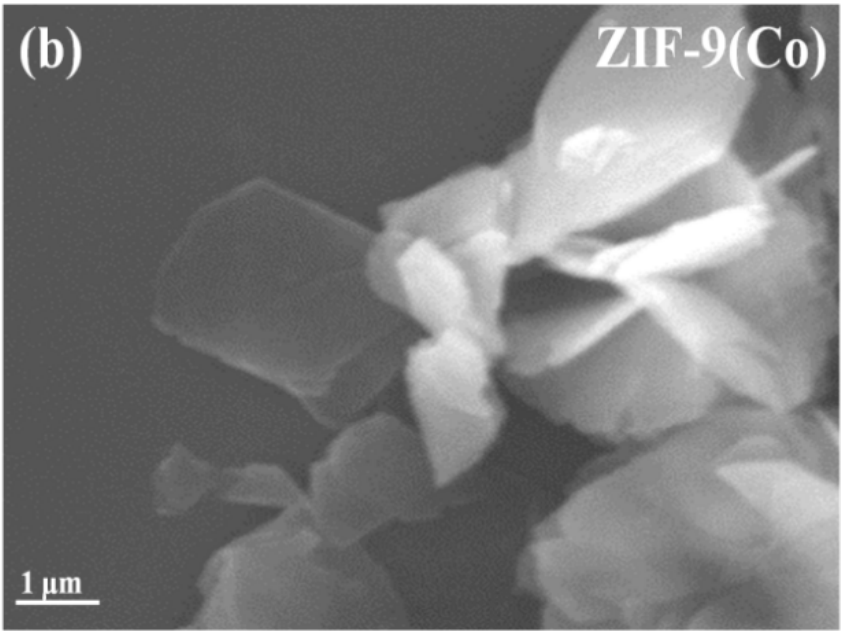

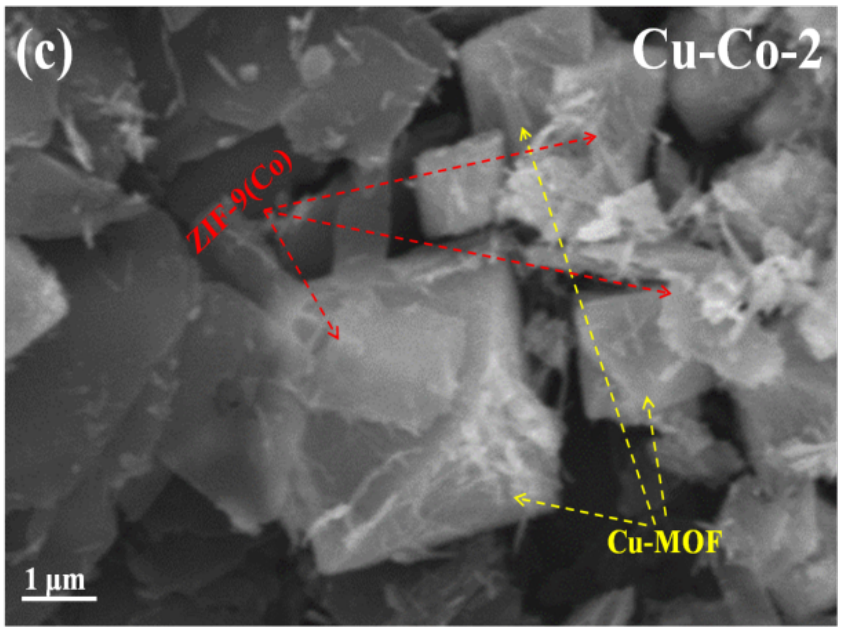

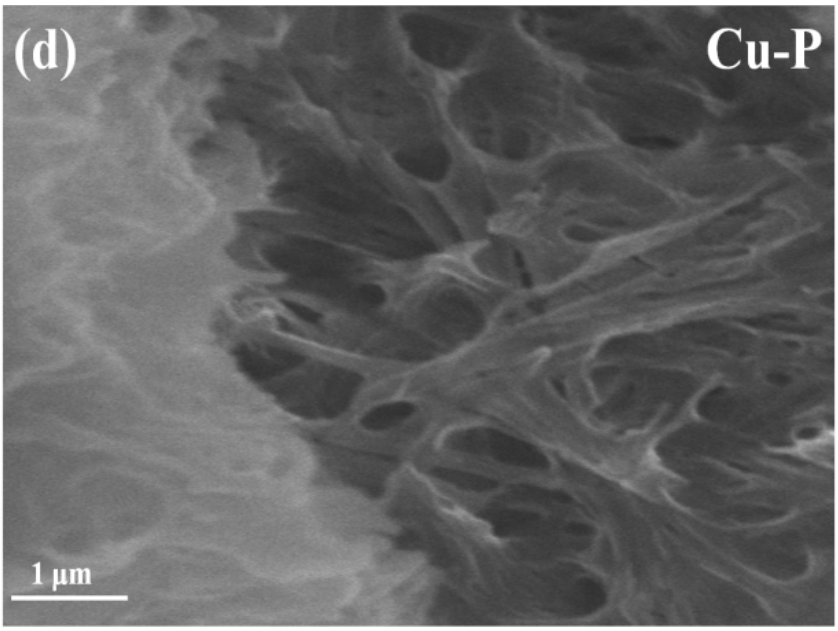

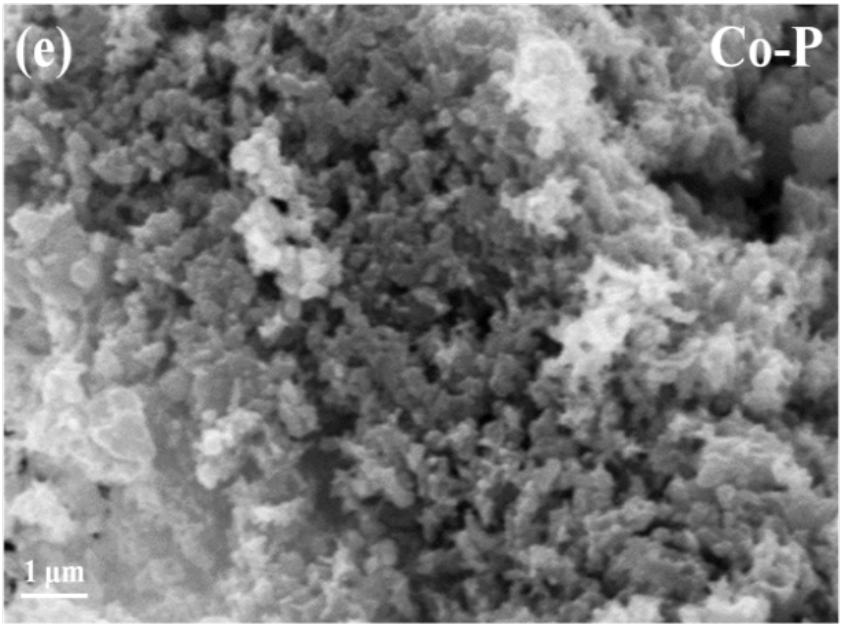

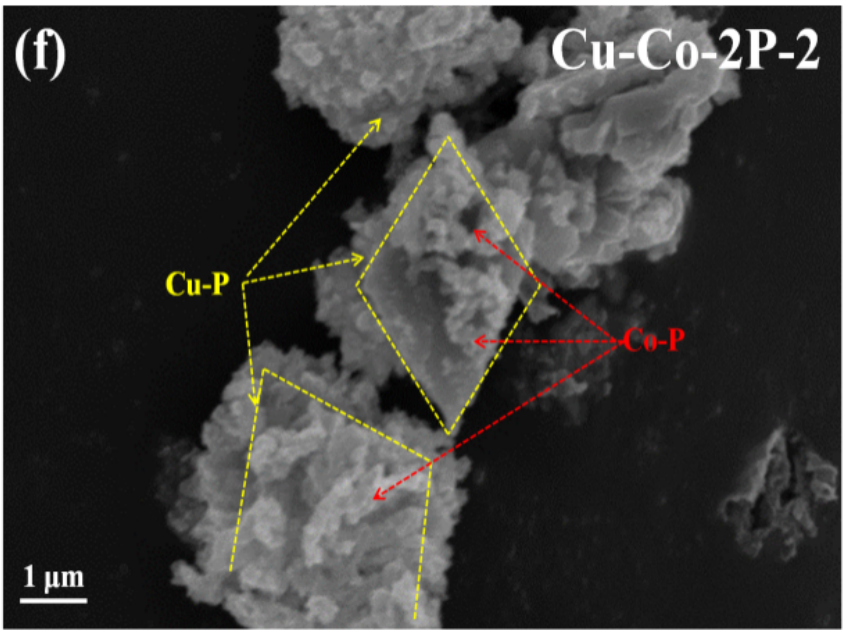

Figure 3. SEM images: (a) Cu-MOFs; (b)ZIF-9(Co); (c) Cu-Co-2; (d)Cu-P; (e)Co-P and (f) Cu-Co-2P-2.

Cu-Co-2P-2 composite photocatalyst was tested by TEM characterization to further understand the morphology and microstructure of the catalyst. Figure 4(a) and Figure S2(a, b) show the TEM images of Cu-Co-2P-2 composites at different magnifications, respectively. The results showed that Cu-P-2 and broken Cu-MOFs skeletons existed in the Cu-Co-2P-2 sample when Cu-MOFs was not completely phosphated, and obvious transparent sheet-like Co-P appeared on the edges [30]. In addition, the HRTEM image of the Cu-Co-2P-2 composite is shown in Figure 4(b). Cu-MOFs is perfectly combined with Co-MOFs phosphatium phospholipids, and the lattice fringes of Cu_3P and CoP can be observed. The lattice spacings of 0.25 nm and 0.24 nm correspond to the (112) and (111) crystal planes of Cu_3P and CoP, respectively. The existence of Cu (200) crystal plane can be also observed, and its lattice spacing is 0.18 nm. EDX results show that Cu-Co-2P-2 composites contain Cu, Co and P elements (Figure 4(c)). According to XRD analysis, it can be seen that Cu-Co-2P-2 composites obtained after phosphating of Cu-Co-2 samples mainly exist in the form of Cu_3P and CoP. At the same time, the electron diffraction (SAED) pattern of Cu-Co-2P-2 (Figure 4(d)) shows the relatively high crystalline characteristics of the composite sample. Figure 4(e) is a map of Cu-Co-2P-2, in which the elements of Cu, Co, and P are evenly distributed. This shows that the phosphating of Cu-MOFs@ZIF-9(Co) was successful.

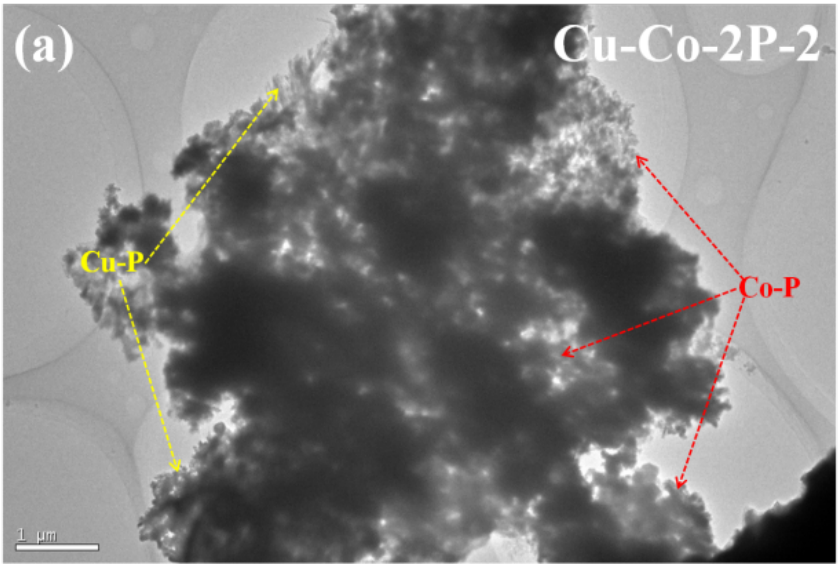

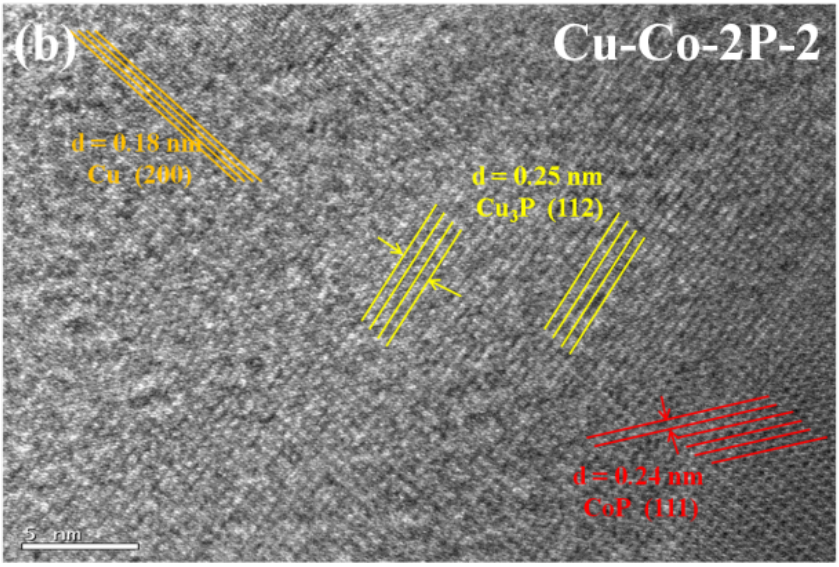

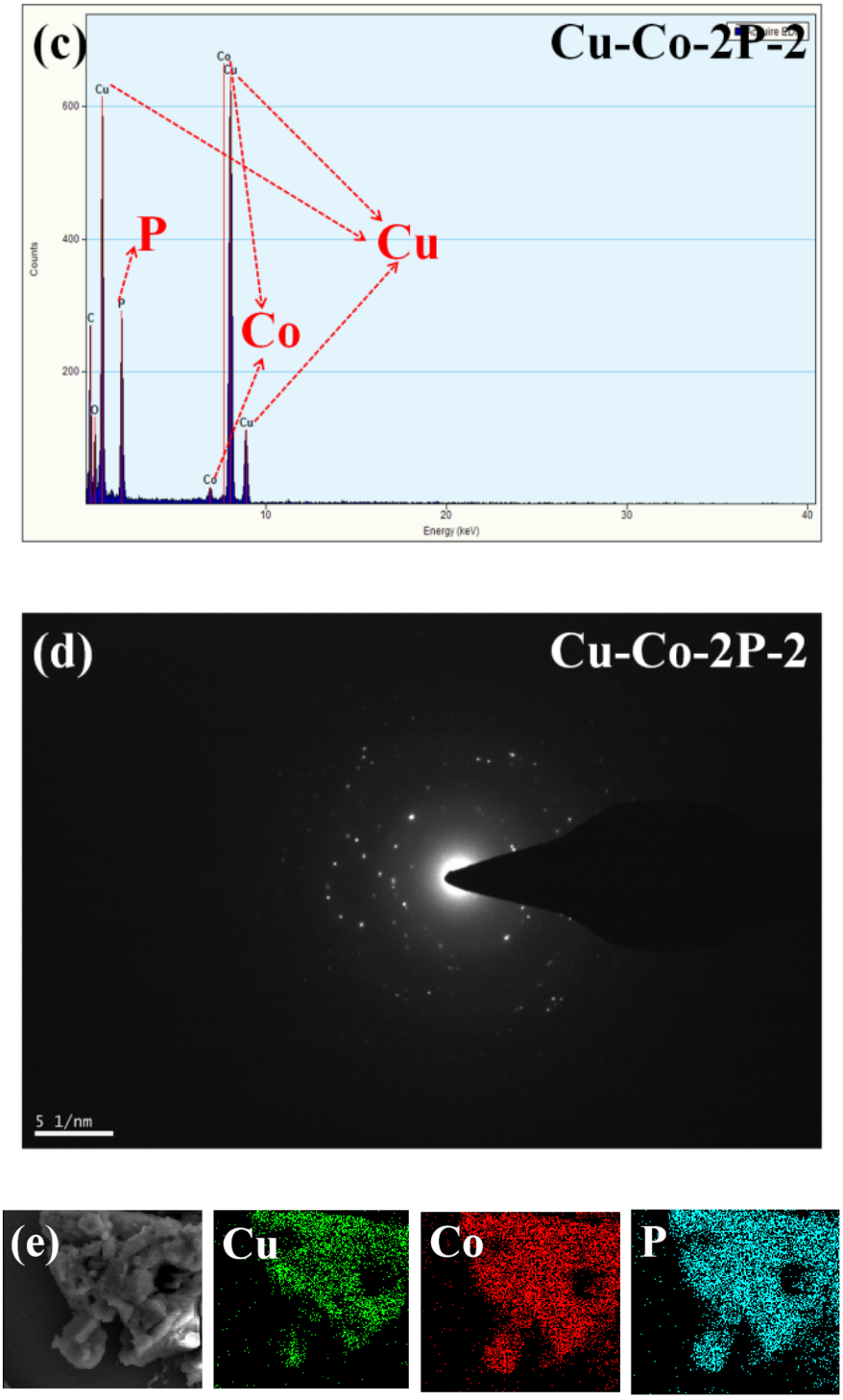

Figure 4. (a) TEM image; (b) HRTEM image; (c) EDX image; (d) SAED pattern and (e) element mapping of Cu-Co-2P-2.

Figure 5 shows the X-ray photoelectron spectroscopy (XPS) of Co-P, Cu-P and Cu-Co-2P-2. The XPS measurement spectra of Co-P, Cu-P and Cu-Co-2P-2 and the corresponding high-resolution XPS spectra of

various elements are shown in Figure 5(a). It can be easily seen from Figure 5(a) that MOFs derived Co-P and Cu-P photocatalysts contain Na, C, N and O. And Cu-Co-2P-2 composite photocatalysts have both Cu and Co signals. Figures 5(b, c and d) are high-resolution XPS spectra of Co 2p, Cu 2p, and P 2p respectively. Figure 5(b) shows the Co 2p peaks of Co-P and Cu-Co-2P-2, respectively. The peak at 793.1eV is assigned to Co $2p_{1/2}$, and the binding energy values of 778.1 eV and 777.9 eV correspond to Co $2p_{3/2}$. In addition, the diffraction peaks at 779.9 eV and 800.1 eV/799.9 eV belong to the vibration satellites of Co $2p_{3/2}$ and Co $2p_{1/2}$ [31]. From pure CoP toCu_3P@CoP composite, Co $2p_{3/2}$ binding energy has a negative shift to lower binding energy. These observations indicate that there is a strong electronic interaction between CoP and Cu_3P in Cu-Co-2P-2, which is of great significance for promoting photocatalytic hydrogen production activity. The test results of the Cu-P photocatalyst obtained by fully phosphating Cu-MOFs are shown in Figure 5(c). The high-resolution XPS of Cu-P shows four peaks, two peaks corresponding to the $2p_{3/2}$ and Cu $2p_{1/2}$ spin states at 932.6 and 952.5 eV, respectively. The two peaks at 933.5 and 955.3 eV are satellite peaks [32]. In the Cu-Co-2P-2 sample, since the Cu-MOFs inside are only partially phosphorylated, the binding energy of the Cu 2p orbital is different from that of the Cu 2p orbital in the Cu-P sample. In the same Cu-Co-2P-2 sample, the binding energies of Cu $2p_{3/2}$ and Cu $2p_{1/2}$ are divided into 932.5 and 952.7 eV. The peak at 936.2 eV is a satellite peak in 2P orbit, and the broad peak with binding energy value of 944.8 eV is related to incompletely phosphated Cu-MOFs [33]. The XPS spectrum of the P 2p energy level is shown in Figure 5(d). The high-resolution XPS spectrum of the element P of Cu-P, Co-P and Cu-Co-2P-2 samples can be divided into two peaks. The three signals with a binding energy of 133.7eV (Cu-Co-2P-2), 133.5eV (Cu-P) and 133.4 eV (Co-P) are resulted from the surface oxidation of the sample when it contact with air, which is an oxidized P species [32, 34]. The three peaks at 129.5 eV (Cu-Co-2P-2), 129.1 eV (Cu-P) and 129.4 eV (Co-P) correspond to the binding energy of the M-P (M = Cu, Co) bond, indicating the formation of metal phosphides. It is impressive that the peaks of Cu-Co-2P-2 both shift to a high binding energy compared with Co-P and Cu-P. These results further indicate that there is a strong electronic interaction between Cu_3P and CoP in Cu-Co-2P-2, which is beneficial for improving the catalytic performance of the composite photocatalyst [35].

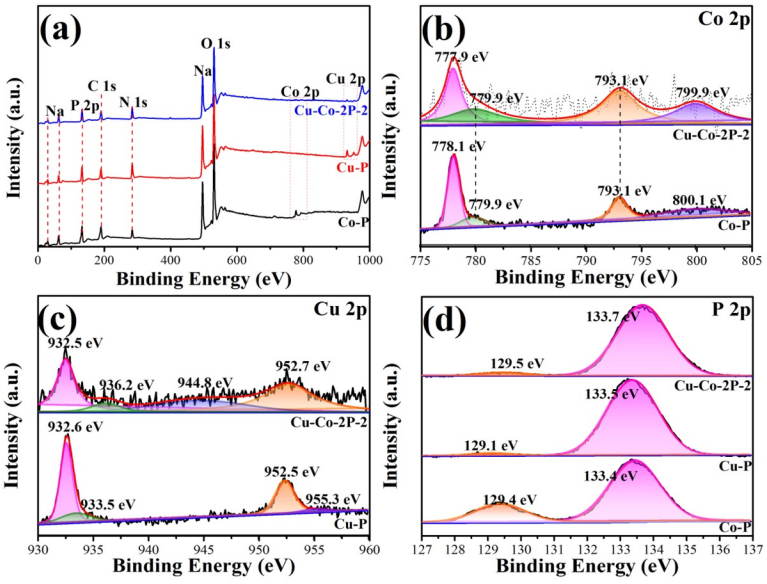

Figure 5. (a) XPS spectra of Co-P, Cu-P and Cu-Co-2P-2; (b) Co 2p spectra of Co-P and Cu-Co-2P-2; (c) Cu 2p spectra of Cu-P and Cu-Co-2P-2; (d) P 2p spectra of Co-P, Cu-P and Cu-Co-2P-2.

In addition, the results of Brunauer-Emmett-Teller (BET) tests can also prove the effect of incompletely

phosphated Cu-MoF on composites. The nitrogen adsorption-desorption isotherms tested at 77 K obtain pore volume, pore size, and porosity and the results are shown in Table S1 and Figure S3. The isotherms of Co-P, Cu-P and partially phosphatized Cu-Co-2P-2 materials produced by fully phosphating belong to the IV isotherm [36]. It has a H3 type hysteresis loop under relatively high pressure, which means that the mesoporous material has a multi-layer adsorption process due to capillary condensation. It is worth noting that Cu-Co-2P-2 material has the highest specific surface area, largest pore volume and average pore diameter.

The excellent light absorption performance of the photocatalyst is a sufficient condition to ensure efficient photocatalytic activity. The photocatalysts were tested in the UV-Vis-NIR DRS (200-800nm) before and after phosphating. The diffuse reflection spectra of ZIF-9(Co), Cu-MOFs and Cu-MOFs@ZIF-9(Co) samples before phosphating are shown in Figure S4(a). Unphosphorylated pure ZIF-9 (Co) has strong absorption in 400-650nm, while pure Cu-MoF is a blue powder and therefore also has strong absorption in the range of 500-800 nm. The Cu-MOFs@ZIF-9(Co) sample has strong absorption in the visible near-infrared region. The successful assembly of Cu-MOFs and ZIF-9 is explained from the side. Figure S4(b) shows the diffuse reflectance spectra of the Co-P, Cu-P and Cu-Co-2P-2 samples obtained from phosphating. The samples all show strong optical absorption density. Absorption in the ultraviolet and near infrared regions means that the catalyst can achieve electronic transitions at higher or lower energies. The stronger light absorption capacity of photocatalyst means the stronger probability of electron transfer under light, which is more favorable for H_2 evolution [37, 38]. Co-P, Cu-P and Cu-Co-2P-2 samples continue to maintain high levels of absorbance with increasing wavelength, which means that light energy is more utilized [39]. This is the important reason why both Co-P and Cu-P show a certain photocatalytic activity. The Cu-Co-2P-2 sample has the highest optical absorption density, which indicates that the strong light absorption performance of the black sample may be the main reason for its enhanced hydrogen evolution activity.

3.2 Photocatalytic hydrogen evolution activity of the catalyst

The photocatalytic hydrogen production reaction of the catalyst was performed in a reaction system of 15 vt% triethanolamine as a sacrificial reagent. The use of EY sensitizer enhances the catalyst's ability to absorb light. In the dark state (without light), no hydrogen was generated in all samples. The activity ratio experiments of composite photocatalysts with different ratios and degrees of phosphatization were performed in TEOA solution at pH = 10. It can be clearly seen from Figure 6(a) that Cu-P and Co-P produced by complete phosphation of Cu-MOFs and ZIF-9(Co) show a certain photocatalytic hydrogen release activity, and the activity of Co-P is better than that of Cu-P. The photocatalytic activity of Cu-Co-xP-2 (x = 1, 2, 3, 4 .) composite photocatalysts was obtained from Cu-MOFs@ZIF-9(Co) composites with different degrees of phosphating treatment, as shown in Figure 6(b). Under EY sensitized conditions, the in-situ phosphation was used to control the phosphorization of the Cu-MOFs@ZIF-9(Co) core-shell structure. The results show that the photocatalytic activity of the composite catalyst constructed by introducing a certain amount of P on the surface of Cu-MOFs@ZIF-9(Co) has been significantly improved. The activity of Cu-Co-1P-2 and Cu-Co-2P-2 samples was significantly improved during slight phosphating. However, after further phosphating, the activity of Cu-Co-3P-2 and Cu-Co-4P-2 composite photocatalysts began to decrease. Combined with XRD (Figure 2(c)), it can be seen that the production of CoP on the surface of Cu-MOFs@ZIF-9(Co) and the exposure of unphosphorylated Cu-MoFs on the inner layer are the main reasons for the change in the activity of the composite photocatalyst. In order to adjust the internal and external phosphating ratio of Cu-MOFs@ZIF-9(Co) core-shell structure, Cu-Co-x (x = 1, 2, 3, 4.) materials with different Cu-Co ratios were constructed by adjusting the amount of Cu-MOFs. Cu-Co-2P-x (x = 1, 2, 3, 4.) photocatalyst was obtained under the same phosphating treatment. As shown in Figure 6(c), the hydrogen-producing activity of Cu-Co-2P-x (x = 1, 2, 3, 4.) composite catalysts with different contents of Cu-MOFs was explored. The highest hydrogen-producing activity was the Cu-Co-2P-2 photocatalyst. With the increase of Cu-MOFs content, the phosphatization degree of the whole sample also increased, so there is almost no Cu-MOFs peak in Cu-Co-2P-4. It can be seen that the excellent photocatalytic activity of Cu-Co-2P-2 composite catalyst can be derived from two aspects, on the one hand, the synergistic effect of CoP and Cu_3P,which were derived from MOFs phosphation, play an important role. On the other hand, because the nucleated

Cu-MOFs is not completely phosphated, it retains the three-dimensional structure as a reaction carrier. We further explored the effect of pH of system on the catalytic activity of Cu-Co-2P-2 composite photocatalyst. It can be seen from Figure 6(d) that the Cu-Co-2P-2 composite photocatalyst exhibits different selectivity to the reaction environment and has the best activity at pH = 10. This shows that a mild alkaline environment is the most favorable factor for a hydrogen production system [29]. The system with extra acid orbase is not conducive to theprocess of the hydrogen precipitation reaction [30]. This is because the neutral solution contains a large amount of H^+, which may cause the protonation of the triethanolamine solution and serious decrease of the electron donor effectiveness [38, 39]. When the reaction conditions become strongly basic, the thermodynamic driving force for hydrogen evolution is obviously insufficient due to the lack of H^+ [40]. In addition, the adsorption of EY molecules on the photocatalyst is also affected by the solution pH of the reaction system.

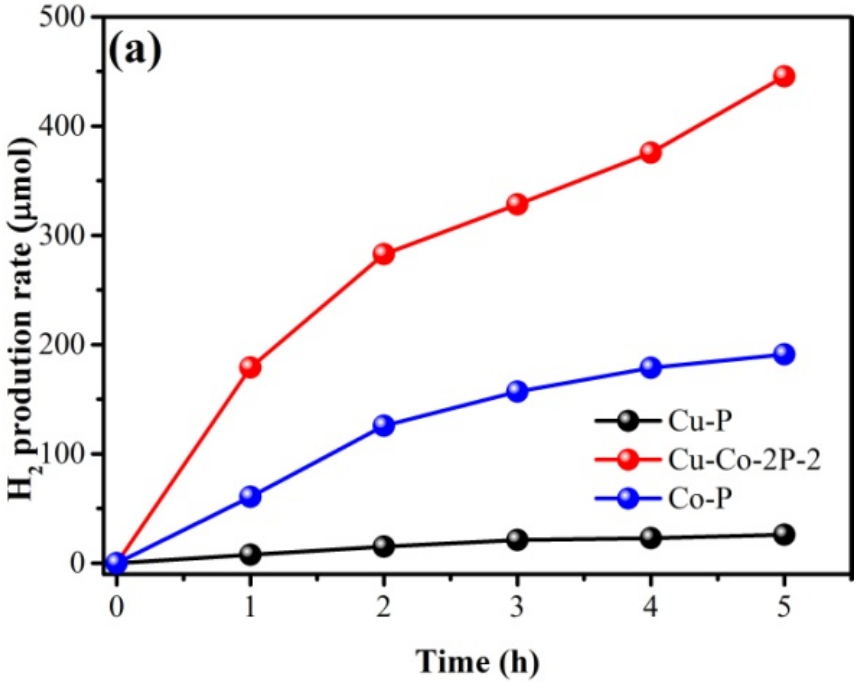

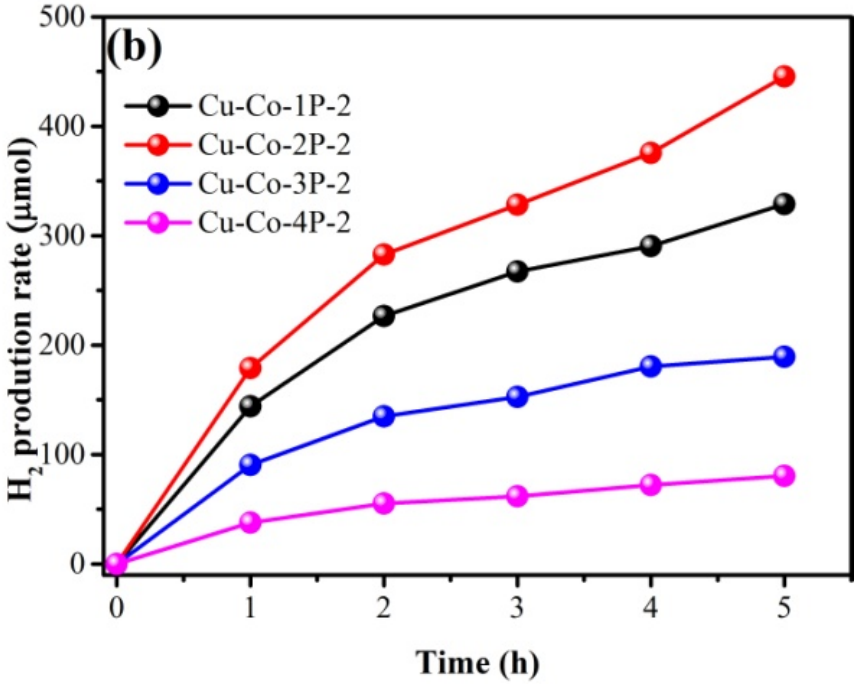

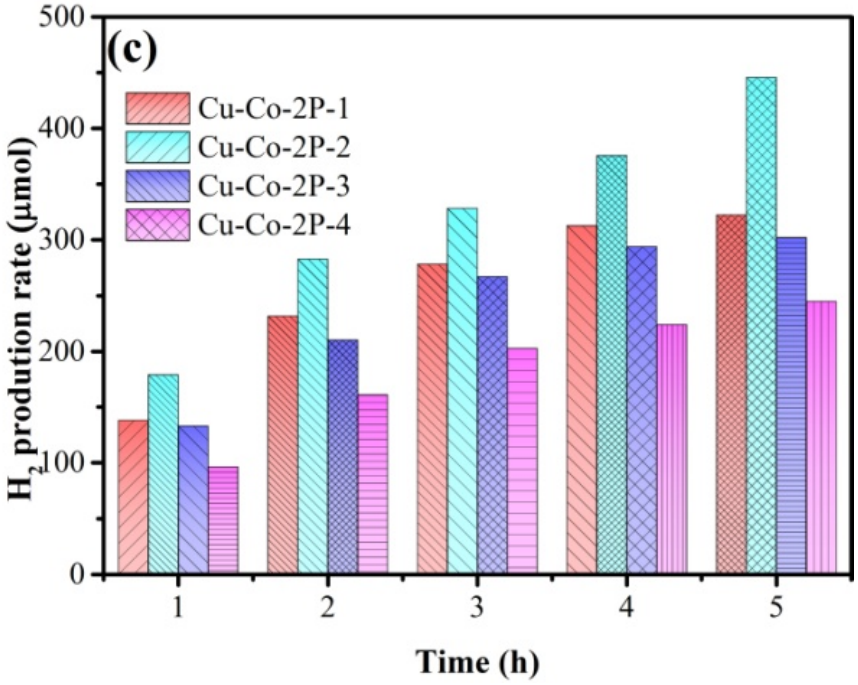

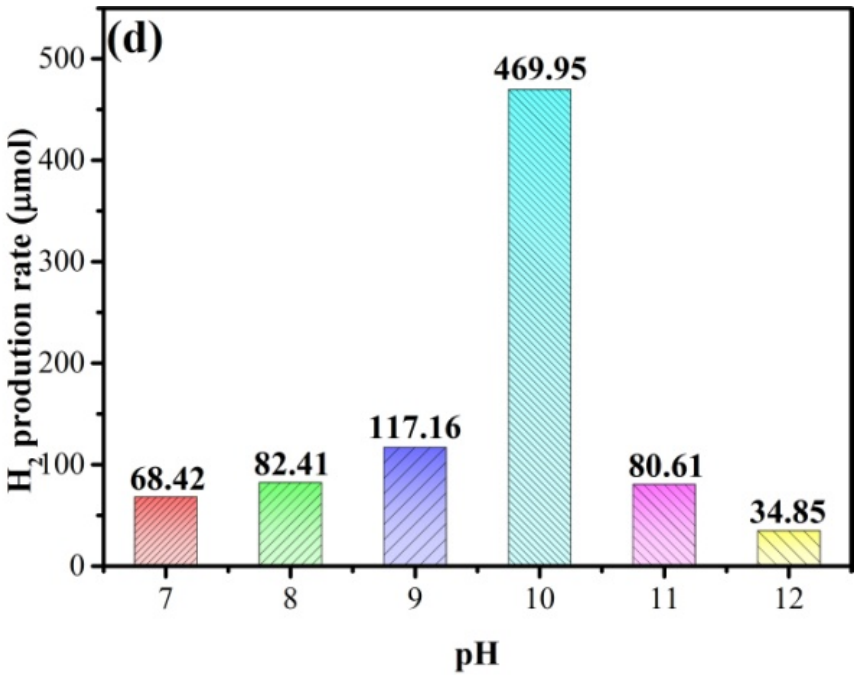

Figure 6 . (a) Comparison of hydrogen evolution of CuP, CoP and Cu-Cu-2P-2 catalyst samples; (b) Comparison of hydrogen production activities of catalysts with different phosphating degrees; (c) Comparison of hydrogen production activities of different Cu-MOFs catalysts; (d) Effect of triethanolamine aqueous solution with different pH on the photocatalytic activity of Cu-Co-2P-2.

The cyclic stability of photocatalysts is very important for their applications. As shown in Figure 7, there is Cu-Co-2P-2 composite photocatalytic activity test comparison for four cycles in consecutive 20 h. The catalyst and sacrificial reagent were not re-added during the entire experiment. 10 mg of EY is added to the reaction flask again at each regassing. Stability tests show that the total amount of produced hydrogen is only slightly reduced at the end of each cycle. This is mainly because the adsorbed EY dye is easily desorbed and diffused into the solution, and the catalyst has slight photo-induced corrosion [38, 40, 41]. Compared with the first cycle, the fourth cycle is only down by 13.7%, which indicates that the Cu-Co-2P-2 photocatalyst has excellent cycle stability and certain application prospects.

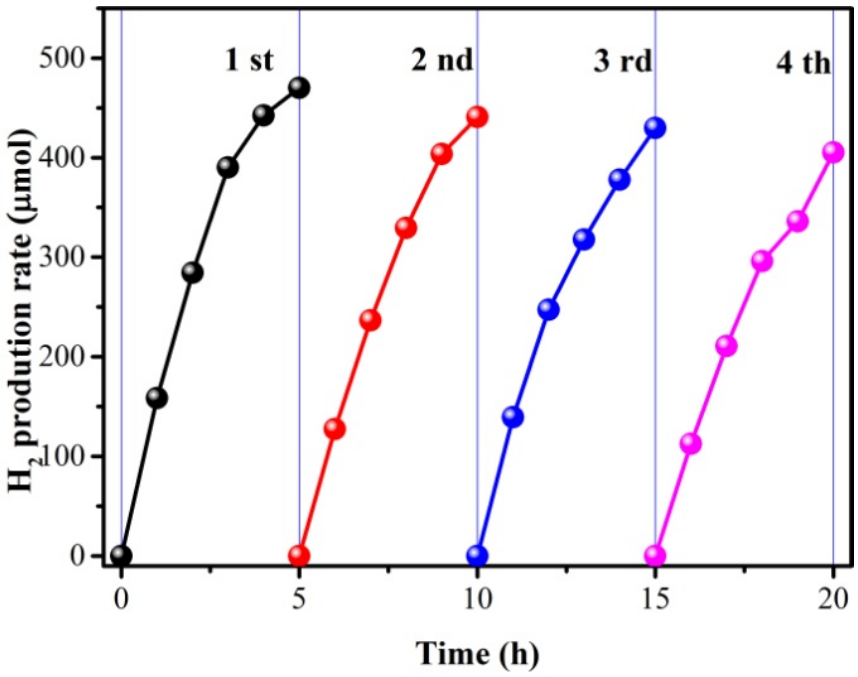

Figure 7 . (d) Cu-Co-2P-2 photocatalyst stability test curve

3.3 Photoluminescence analysis

The steady-state fluorescence spectrum was used to test the fluorescence performance of the catalyst in EY solution, and the electron transfer and excited state interactions between EY and photocatalyst were discussed. As shown in Figure 8(a), the pure EY solution produces the strongest fluorescence under the excitation of 480 nm light. Different fluorescence intensity indicates different degrees of electron-hole recombination. When the fluorescence intensity is higher, the peak value is higher, showing that the number of excited electrons returned to the ground state by radiation decay transition is higher, which leads to higher electron recombination rate [42, 43]. With the addition of photocatalyst materials, the signal decreases, indicating that the recombination rate of electron-hole pairs is reduced [44], and it is also shown that the electron-hole pair recombination of the catalyst is suppressed [45, 46]. Figure S5(a) shows the steady-state fluorescence curves of Cu-MOFs@ZIF-9 catalysts with different degrees of phosphatization. The Cu-Co-2P-2 photocatalyst has the lowest fluorescence peak intensity, indicating that the recombination rate of electron-hole pairs in Cu-Co-2P-2 is most significantly reduced. After adjusting the amount of internal Cu-MOFs, the fluorescence pattern of Cu-Co-2P-x (x = 1.2.3.4) prepared under the same phosphating conditions is shown in Figure S5(b). With the increase of the mass of Cu-MOFs, the intensity of the fluorescence peak decreases at first and then increases. This indicates that thereexists a good ratio of Cu-MOFs to ZIF-9(Co) and good phosphation degree while preparing the composite photocatalyst. At the same time, in order to further test the fluorescence performance of Cu-Co-2P-2 catalyst, it was also compared with Cu-P and Co-P derived from pure Cu-MOFs and Co-MOFs. The results are shown in Figure 8(a). In Cu-Co-2P-2 composite samples, the presence of Cu_3P@CoP p-n type heterojunctions greatly promotes electron transport and improves charge separation efficiency, so the fluorescence peak intensity is the lowest.

The dynamic conditions of photogenic carriers were detected by transient fluorescence, as shown in Figure 8(b) and Figure S5(c, d). The corresponding time resolved photoluminescence (TRPL) was fitted by using

the three-exponential attenuation model.

$$\mathbf{I(t) = B + \sum_{i=1,\ 2,\ 3} A_i\ e^{\frac{-t}{\tau_i}}} \qquad (1);$$

τ is emission $lifetimes$; A is the corresponding amplitude.

The transient fluorescence lifetimes of Cu-P, Co-P and Cu-Co-P semiconductor catalysts are shown in Table 1. It can be clearly seen that due to the interaction between the dye molecule EY and the photocatalyst, the formed complex has weak fluorescence. At the same time, in order to gain deeper understanding the reasons for different phosphatization degrees and the difference in hydrogen production activity of various precursor ratios,instantaneous fluorescence test of Cu-Co-xP-2 and Cu-Co-2P-x (x = 1. 3. 4.) composite catalyst have been alsodone, and correlated analysis results are shown in Table S1.

The average life (τ_{ave}) can be calculated by formula (2):

$$< \tau_{ave} > \ = \ \frac{\sum_{i=1,\ 2,\ 3} A_i\ \tau_i^2}{\sum_{i=1,\ 2,\ 3} A_i\ \tau_i} \qquad (2);$$

τ is emission $lifetimes$; A is the corresponding amplitude.

It is clear from Table 1 and Table S2 that the average lifespan of all samples varies widely. The simple EY life is 0.3579 ns, and the average life has been greatly improved after adding the photocatalyst material. The average lifetimes of Cu-P and Co-P are 0.2831 ns and 0.2884 ns, respectively. In particular, Cu-Co-2P-2 composites have the lowest average lifetime of 0.1325 ns, which indicates that Cu_3P@CoP p-n type heterojunctions can enhance electron transfer and significantly reduce the recombination of photogenerated charges [46].

The electron transfer rate constant is calculated by formula (3).

$$\mathbf{k_{et} = \frac{1}{\tau_{F,s}} - \frac{1}{\tau_{F,l}}} \qquad (3).$$

k_{et} $is\ electron\ transfer\ rate\ constants$; $\tau_{F,s}$ $is\ short\ lifetimes$; $\tau_{F,l}$ is long lifetimes.

Based on the difference between the long life and short life of the carriers in the sample, the specific charge transfer rate constants (k_{et}) of all the catalyst samples are calculated in Table 1 and Table S2. The k_{et} of Cu-Co-2P-2 is 1.198×10^{10}, which is the largest among all catalysts. The maximum transfer rate means the fastest photo-generated charge transfer, the lowest recombination efficiency of photo-generated carriers, and the highest photocatalytic activity of hydrogen evolution. This is consistent with the results of the hydrogen evolution kinetics.

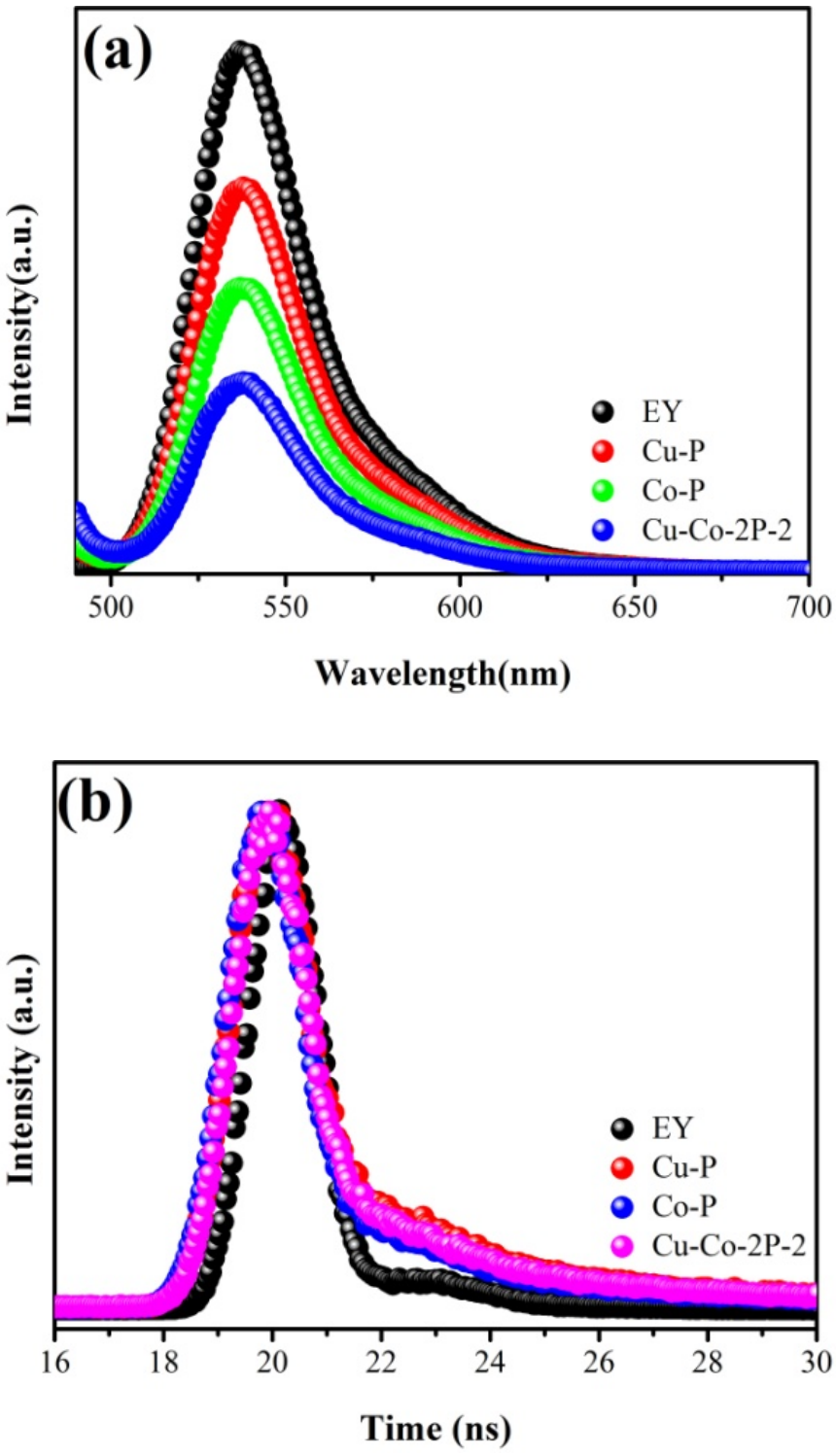

Figure 8. Steady-state (a) and transient fluorescence spectra (b) of Cu-P, Co-P, and Cu-Co-2P-2.

Table 1. Attenuation parameters of Cu-P, Co-P, and Cu-Co-2P-2.

Samples	Pre-exponential factors A	Λιφετιμε, <τ> (νς)
	A_1=15.43	τ_1=3.303
Cu-Co-1P-2	A_2=4.64	τ_2=39.16
	A_3=79.92	τ_3=0.2626
	A_1=13.62	$\tau_{1=}$4.154
Cu-Co-3P-2	A_2=10.48	τ_2=107.3
	A_3=75.90	τ_3=0.1669
	A_1=11.57	$\tau_{1=}$4.267
Cu-Co-4P-2	A_2=7.29	τ_2=98.07
	A_3=81.14	τ_3=0.1700
	A_1=13.93	$\tau_{1=}$4.154
Cu-Co-2P-1	A_2=10.02	τ_2=106.3
Cu-Co-2P-3 Cu-Co-2P-4	A_3=76.05 A_1=15.29 A_2=7.12 A_3=77.59 A_1=15.63 A_2=6.01 A_3=78.35	τ_3=0.1617 τ_1=4.016 τ_2=

3.4 Photoelectrochemical characterization test

Generally, the photocurrent response is used to reveal the photoelectrochemical properties that occur on the photocatalyst surface [47, 48]. Figure 9(a) shows the photocurrent response curves of Cu-P, Co-P and Cu-Co-2P-2. Compared with Cu-P and Co-P samples, Cu-Co-2P-2 showed the highest photocurrent density. This high photocurrent density further indicates that the photogenerated carriers in the partially phosphated Cu-MOFs@ZIF-9 composite catalyst with a special structure have a more effective separation efficiency and a lower recombination rate, thereby enhancing the photocatalytic H_2 Production activity. The polarization curves were used to explore the changes in the current density of Cu-P, Co-P, and Cu-Co-2P-2 as a function of voltage and the level of hydrogen production overpotential.

The LSV curves of Cu-P, Co-P and Cu-Co-2P-2 electrodes are shown in Figure 9(b). Unsurprisingly, Cu-Co-2P-2 showed the fastest increase in current density, indicating that Cu-Co-2P-2 has a lower overpotential. The decrease of the hydrogen-producing overpotential was mainly due to the rapid electron transfer at the layered Cu-P@Co-P interface, which indicates that Cu-Co-2P-2 composite catalyst has strong HER activity.

Electrochemical impedance spectroscopy (EIS) plots were collected at open circuit potentials in the frequency range of 1 MHz to 0.1 Hz. As shown in Figure 9(c), the size of the curvature radius of the curve reflects the size of the charge transfer resistance. The relatively small circular orphan indicates that the charge transfer is faster [47]. Cu-Co-2P-2 has the smallest radius of curvature, indicating its excellent electrical conductivity. The combination of Co-P and Cu-P constitutes a rapid transfer channel. Therefore, the Nyquist curve of Cu-Co-2P-2 composites shows a significantly reduced semicircle, which indicates that the charge transfer rate of Cu-Co-2P-2 composites is significantly enhanced.

The Mott-Schottky tests of Co-P, Cu-P and Cu-Co-2P-2 are shown in Figure 9(d-f). The positive and negative slope of the curve in the figure can be used as a basis for judging the type of semiconductor. The slope is a regular description of an n-type semiconductor, otherwise it is a p-type semiconductor. Pure Co-P in Figure 9(d) has a positive slope, which is typical n-type semiconductor behavior. The slope of pure Cu-P is negative, indicating that Cu_3P is a p-type semiconductor. The flat band potentials (E_{fb}) for Cu-P and Co-P are estimated at 1.21 V and -0.45 V, respectively, which are relative to SCE. According to the meaning of the flat band potential, the Fermi level (E_f) position of pure CoP and pure Cu_3P samples can also be roughly estimated. Generally, the conduction band potential (E_{CB}) of an n-type semiconductor is more negative -0.1 or -0.2 V than its flat band potential [47, 49], while the valence band potential of a p-type semiconductor is corrected by 0.1 or 0.2 V. Therefore, the Co-P conduction band is roughly estimated to be -0.65 V, and the Cu-P valence band is roughly estimated to be 1.41 V relative to SCE. For the Cu-Co-2P-2 composite catalyst, there are two linear regions in the Mott-Schottky diagram, which can be attributed to the flat band potentials of the recombined CoP and Cu_3P, the values of which are -0.07 V and 1.02 V, respectively. This

is due to the formation of a p-n heterojunction after the recombination of n-type CoP and p-type Cu_3P, which results in a Fermi level shift, that is a shift in the flat band potential.

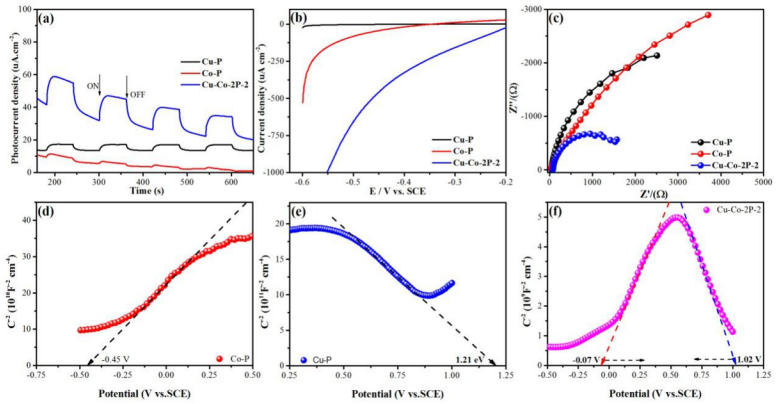

Figure 9 . (a) Transient photocurrent response; (b) LSV curves; (c) Nyquist plots for Cu-P, Co-P and Cu-Co-2P-2 samples; Mott-Schottky plots for Cu-P (d), Co-P (e) and Cu-Co-2P-2 (f) samples.

3.5 Proposed photocatalytic mechanism

Based on Mott-Schottky's test results, the band structure of CoP and Cu_3P can be further analyzed. The band gap energies of pure CoP and Cu_3P can be obtained from the literature [24, 50, 51], which are 1.74 eV and 1.55 eV, respectively. The valence band of CoP and theconduction band of Cu_3P can be obtained through the formula of $E_{VB} = E_{CB} + E_g$, whose values are 1.09 V and -0.14 V, respectively. Therefore, before and after the contact, the band positions of p-Cu_3P and n-CoP are shown in Figure 10(a). Because p-type semiconductors have Fermi levels close to VB, n-type semiconductors have Fermi levels close to CB [52]. After the contact between p-Cu_3P and n-CoP, due to the existence of the potential difference, an electric field was built in the semiconductor to promote charge transfer. During the formation of the p-n heterojunction, when the Fermi levels of CoP and Cu_3P reached equilibrium, the direction of this internal electric field was directed from CoP to Cu_3P [53]. At the same time, the conduction band of Cu_3P will increase, and the conduction band of CoP will decrease with the action of Fermi leverage until the Fermi energy levels of CoP and Cu_3P reach the equilibrium [54], which is also confirmed from two linear regions in the Mott-Schottky of Cu-Co-2P-2 composite catalyst.

Under visible light, CoP and Cu_3P semiconductors absorb enough energy to generate electron-hole pairs under the action of EY sensitization. The EY molecule as a sensitizer is adsorbed on the surface of the photocatalyst to form a single excited state EY^{1*} under visible light irradiation, and then undergoes a band gap conversion to form a more stable triple excited state EY^{3*}. With TEOA as the electron donor, EY^{3*} is reduced and quenched to form $EY^{-\cdot}$ with strong reducing ability. The electrons of $EY^{-\cdot}$ are transferred to the surface of the composite photocatalyst and participate in the reduction reaction to precipitate H_2. At the same time, the dye molecules return to the ground state. The incompletely phosphatized MOFs framework provides a support for CoP and Cu_3P produced by Cu-MOFs@ZIF-9(Co) phosphating, making dye molecules more easily adsorbed on the semiconductor surface. An interfacial electric field was formed in a p-n junction composite catalyst constructed by Cu_3P and CoP, and the direction was from n-type CoP to p-type Cu_3P [54]. CoP and Cu_3P are excited by visible light, and electrons and holes are generated. The electrons transition from the valence band (VB) of the photocatalyst to the conduction band (CB). Then, under the

action of the interface electric field, the electrons on the CB of Cu_3P quickly migrate to the CB of CoP, and then participate in the hydrogen evolution reaction of reduced water. At the same time, the holes migrate from the VB of CoP, to the VB of Cu_3P, and are finally consumed by TEOA molecules. It is worth mentioning that the generated $EY^{\cdot-}$ fluorene molecules with strong reducing ability during EY sensitization can transfer electrons to the conduction band of CoP and Cu_3P, providing a rich electron source for the reaction system. In the process of photocatalytic water splitting, the pn heterojunction formed by the combination of CoP and Cu_3P effectively promotes the transfer of electrons and greatly inhibits the recombination of electron-hole pairs, thereby significantly improving the photocatalytic hydrogen production activity.

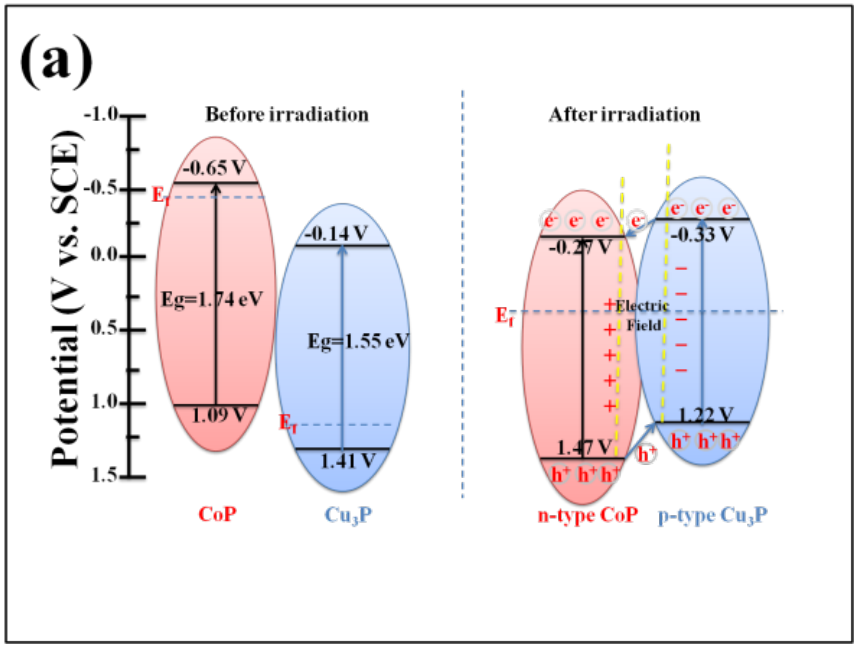

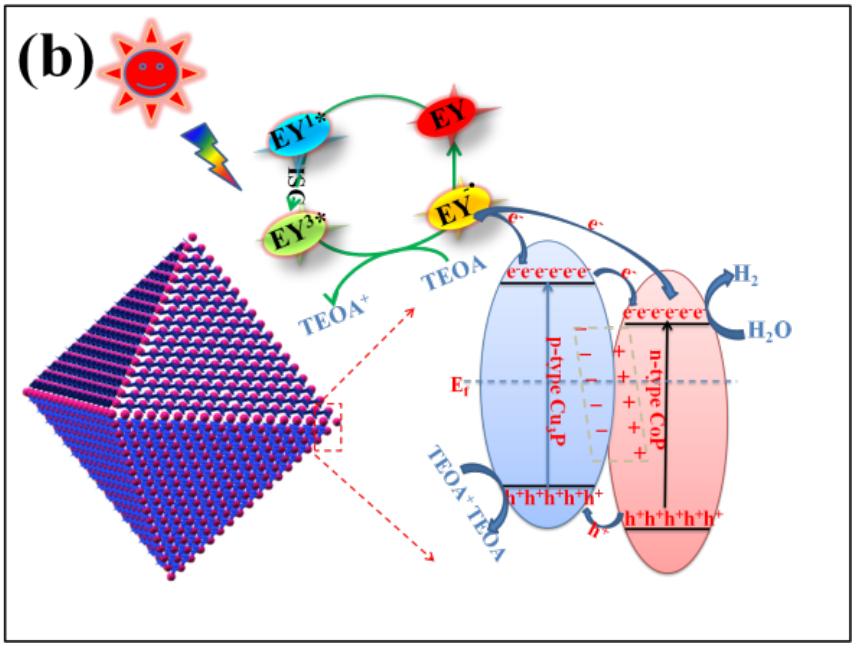

Figure 10 . (a) Charge transfer mechanisms over p-n heterojunction of Cu_3P@CoP under visible light irradiation; (b) Mechanism diagram of the hydrogen production process by water decomposition of EY-sensitized Cu-Co-2P-2.

4. Conclusion

In this work, we developed a novel in-situ growth scheme to construct the Cu-MOFs@ZIF-9(Co) core-shell precursor material. The Cu-MOFs@ZIF-9(Co) core-shell precursor was treated by low-temperature phosphorization to obtain a Cu_3P@CoP composite catalyst with a self-supporting structure. The composite Cu-Co-2P-2 was obtained by controlling the phosphation degree of Cu-MOFs@ZIF-9(Co) precursor and adjust the ratio of Cu and Co, and Cu-Co-2P-2 composite had the highest hydrogen production activity reaching 469.95μmol within 5 h. Experiments to control the degree of phosphation of Cu-MOFs@ZIF-9(Co) precursor material and adjust the ratio of Cu to Co show that the photocatalyst recorded as Cu-Co-2P-2 has the highest hydrogen production activity, reaching 469.95 μmol in 5h. The unique structure and composition of Cu_3P@CoP can promote charge migration, provide large surface area and rich active sites to drive water photolysis. Cu_3P@CoP composite catalyst not only has a layered structure, but also builds a p-n heterojunction at the interface of Cu_3P and CoP. The results of photoelectrochemical and fluorescence tests showed that the proper conduction and valence band positions of Cu_3P and CoP formed a more effective path way for the thermodynamic charge transfer. The results further emphasize the importance of material design based on proper energy level locations. This work will promote the design of transition metal phosphide semiconductor devices and further development of heterojunction photocatalysts.

Conflicts of interest

The authors declare no competing interests.

Acknowledgements

This work was financially supported by the Chinese National Natural Science Foundation (Grant Nos. 21862002 and 41663012), the Open Project of State Key Laboratory of High-efficiency Utilization of Coal and Green Chemical Engineering, Ningxia University (2019-KF-36), the Graduate Innovation Project of the North Minzu University (YCX19113), the new technology and system for clean energy catalytic production, Major scientific project of North Minzu University (ZDZX201803).

Author contributions

Lijun Zhang and Xuqiang Hao conceived and designed the experiments; Zhiliang Jin and Tiansheng Zhao contributed reagents/materials and analysis tools; and Lijun Zhang wrote the paper.

References

[1] H. H. Ou, P. J. Yang, L. H. Lin, M. Anpo, X. C. Wang, Carbon Nitride Aerogels for the Photoredox Conversion of Water, Angew. Chem. Int. Ed, 2017, 56, 10905-10910.

[2] J. X. Low, J. G. Yu, M. Jaroniec, S. Wageh, A. A. Al-Ghamdi, Heterojunction Photocatalysts, Adv. Mater. 2017, 29, 1601694.

[3] A. Fujishima, K. Honda, Electrochemical Photolysis of Water at a Semiconductor Electrode, Nature, 1972, 238, 37-38.

[4] Z. L. Jin, X. J. Zhang, Y. X. Li, S. B. Li, G. X. Lu, 5.1% quantum efficiency for stable hydrogen generation over eosin-sensitized CuO/TiO_2 photocatalyst under visible light irradiation, Catal. Commun, 2007, 8, 1267-1273.

[5] X. Yan, Z. L. Jin, Y. P. Zhang, H. Liu, X. L. Ma, Controllable design of double metal oxide ($NiCo_2O_4$) modified CdS for efficient photocatalytic hydrogen production, Phys. Chem. Chem. Phys, 2019, 21, 4501-4512.

[6] H. Li, X. Q. Yan, B. Lin, M. Y. Xia, J. J. Wei, B. L. Yang, G. D. Yang, Controllable Spatial Effect Acting on Photo-induced CdS@CoP@SiO Ball-in-Ball Nano-photoreactor for Enhancing Hydrogen Evolution, Nano energy, 2018,47, 481-493.

[7] S. Q. Peng, Y. Yang, J. N. Tan, C. Gan, Y. X. Li. In situ loading of Ni_2P on $Cd_{0.5}Zn_{0.5}S$ with red phosphorus for enhanced visible light photocatalytic H_2 evolution. Appl. Surf. Sci, 2018, 447, 822-828.

[8] C. Xue, H. Li, H. An, B. L. Yang, J. J. Wei, G. D. Yang, NiS_x Quantum Dots Accelerate Electrons Transfer in $Cd_{0.8}Zn_{0.2}S$ Photocatalytic System via rGO Nanosheet "Bridge" towards Superior Visible-Light-Driven Hydrogen Evolution, ACS Catalysis, 2018, 8, 1532-1545.

[9] Q. Z. Wang. J. J. He, Y. B. Shi, S. L. Zhang, T. J. Niu, H. D. She, Y. P. Bi, Z. Q. Lei, Synthesis of MFe_2O_4 (M = Ni, Co)/$BiVO_4$ film for photolectrochemical hydrogen production activity, Appl. Catal. B: Environ, 2017, 214, 158-167.

[10] H. Y. Wang, Z. L. Jin, Boosting photocatalytic hydrogen evolution achieved by rationally designed/constructed carbon nitride with ternary cobalt phosphosulphide, J Colloid Interf Sci, 2019, 548, 303-311.

[11] J. W. Fu, Q. L. Xu, J. X. Low, C. J. Jiang, J. G. Yu, Ultrathin 2D/2D WO_3/g-C_3N_4step-scheme H_2-production photocatalyst, Appl. Catal. B: Environ, 2019, 243, 556-565.

[13] H. X. Jiang, J. L. Zhou, C. X. Wang, Y. H. Li, Y. F. Chen, M. H. Zhang, Effect of Cosolvent and Temperature on the Structures and Properties of Cu-MOF-74 in Low-temperature NH_3-SCR, Ind. Eng. Chem. Res, 2017, 56, 3542-3550.

[14] N. S. Bobbitt, M. L. Mendonca, A. J. Howarth, T. Islamoglu, J. T. Hupp, O. K. Farha, R. Q. Snurr, Chem. Soc. Rev, 2017, 46, 3357-3385

[15] G. H. Li, H. Yang, F. C. Li, J. Du, W. Shi, P. Cheng, Facile formation of a nanostructured NiP_2@C material for advanced lithium-ion battery anode using adsorption property of metal-organic framework, J. Mater. Chem. A, 2016, 4, 9593-9599.

[16] L. T. Yan, P. C. Dai, Y. Wang, X. Gu, L. J. Li, L. Cao, X. B. Zhao, In Situ Synthesis Strategy for Hierarchically Porous Ni_2P Polyhedrons from MOFs Templates with Enhanced Electrochemical Properties for Hydrogen Evolution, ACS Appl. Mater. Interfaces 2017, 9, 11642-11650.

[17] X. Liang, B. X. Zheng, L. G. Chen, J. T. Zhang, Z. B. Zhuang, B. H. Chen, MOF-Derived Formation of Ni_2P-CoP Bimetallic Phosphides with Strong Interfacial Effect toward Electrocatalytic Water Splitting, ACS Appl. Mater. Interfaces 2017, 9, 23222-23229.

[18] M. Yang, J. Y. Xie, Z. Y. Lin, B. Dong, Y. Chen, X. Ma, M. L. Wen, Y. N. Zhou, L. Wang, Y. M. Chai, N-doped FeP nanorods derived from Fe-MOFs as bifunctional electrocatalysts for overall water splitting, Appl. Surf. Sci, 2019, 17, 145096

[19] Z. Q. Li, L. Y. Zhang, X. L. Ge, C. X. Li, S. H. Dong, C. X. Wang, L. W. Yin, Core-shell structured CoP/FeP porous microcubes interconnected by reduced graphene oxide as high performance anodes for sodium ion batteries, Nano Energy, 2017, 32, 494-502.

[20] J. L. Duan, Y. L. Zou, Z. Y. Li, B. Long, Preparation of MOF-derived NiCoP nanocages as anodes for lithium ion batteries, Powder Technology, 2019, 354, 834-841.

[21] C. M. Li, Y. H. Du, D. P. Wang, S. M. Yin, W. U. Tu, Z. Chen, M. K. Kraft, G. Chen, R. Xu, Unique P-Co-N surface bonding states constructed on g-C_3N_4 nanosheets for drastically enhanced photocatalytic activity of H_2evolution, Adv Funct Mater, 2017, 27, 1604328.

[22] L. J. Zhang, Z. L. Jin, Efective Electron-Hole Separation Over Controllable Construction of CdS/Co-Ni-P Core/Shell Nanophotocatalyst for Improved Photocatalytic Hydrogen Evolution Under Visible-Light-Driven, Catal Surv Asia, 2019, 23, 219-230.

[23] Z. L. Jin, Y. K. Zhang, Q. X. Ma, Orthorhombic WP co-catalyst coupled with electron transfer bridge UiO-66 for efficient visible-light-driven H_2 evolution, J Colloid Interf Sci, 2019, 556, 689-703.

[24] Y. B. Li, Z. L. Jin, H. Liu, H. Y. Wang, Y. P. Zhang, G. R. Wang, Unique photocatalytic activities of transition metal phosphide for hydrogen evolution, J Colloid Interf Sci, 2019, 541, 287-299.

[25] Z. J. Wang, Z. L. Jin, H. Yang, X. L. Ma, H. Liu, Synergistic interface phenomena between MOFs, NiPx for efficient hydrogen production, Mol Catal, 2019, 467, 78-86.

[26] Y. K. Yu, C. W. Chen, C. He, J. F. Miao, J. S. Chen, In situ Growth Synthesis of CuO@Cu-MOFs Core-shell Materials as Novel Low-temperature NH_3-SCR Catalysts, ChemCatChem 2019, 11, 979-984.

[27] B. Panella, M. Hirscher, H. Pütter, U. Müller, Hydrogen Adsorption in Metal-Organic Frameworks: Cu-MOFs and Zn-MOFs Compared, Adv. Funct. Mater. 2006, 16, 520-524.

[28] P. Chowdhury, C. Bikkina, D. Meister, F. Dreisbach, S. Gumma, Comparison of adsorption isotherms on Cu-BTC metal organic frameworks synthesized from different routes, Micropor Mesopor Mat, 2009, 117, 406-413.

[29] H. Y. Wang, Z. L. jin, Rational design W-doped Co-ZIF-9 based Co_3S_4 composite photocatalyst for efficient visible-light-driven photocatalytic H_2evolution, Sustain Energ Fuels, 2019, 3, 173-183.

[30] L. J, Zhang, X. Q. Hao, J. K. Li, Y. P. Wang, Z. L. Jin, Unique synergistic effects of ZIF-9(Co)-derived cobalt phosphide and $CeVO_4$ heterojunction for efficient hydrogen evolution, Chinese J Catal, 2020, 41, 82-94.

[31] X. X. Ma, Y. Q. Chang, Z. Zhe, J. L. Tang, Forest-like NiCoP@Cu_3P Supported on Copper Foam as a bifunctional catalyst for Efficient Water Splitting, J. Mater. Chem. A, 2018, 6, 2100-2106.

[32] Z. Wang, H. T. Du, Z. Liu, H. Wang, Abdullah M. Asirid and Xuping Sun, Interface engineering of CeO_2-Cu_3P nanoarray for efficient alkaline hydrogen evolution, Nanoscale, 2018,10, 2213-2217.

[33] Y. Shi, D. Y. Niu, Z. M. Wu, Z. Z. Liu, Q. D. Zhao, W. Xiong, X. Y. Li, Synthesis of Ag/$Cu_3(BTC)_2$composite catalysts and their catalytic performance for NH_3-SCR, China Environmental Sciencece, 2018, 38, 2445-2450.

[34] S. X. Hua, D. Qu, L. An, W. S. Jiang, Y. J. Wen, X. Y. Wang, Z. C. Sun, Highly efficient p-type Cu_3P/n-type g-C_3N_4 photocatalyst through Zscheme charge transfer route, Appl. Catal. B: Environ, 2019, 240, 253-261.

[35] H. T. Du, X. P. Zhang, Q. Q. Tan, R. M. Kong, F. L. Qu, A Cu_3P-CoP hybrid nanowire array: a superior electrocatalyst for acidic hydrogen evolution reactions, Chem. Commun , 2017, 53 , 12012-12015.

[36] L. J. Zhang, G. R. Wang, Z. L. Jin, Growth of $Zn_{0.5}Cd_{0.5}S$/a-Ni$(OH)_2$heterojunction by a facile hydrothermal transformation efficiently boosting photocatalytic hydrogen production, New J. Chem, 2019, 43, 6411-6421.

[37] Q. D. Li, L. Li, P.J. Wu, N. Xu, L. Wang, M. Li, A. Dai, K. Amine, L.Q. Mai, J. Lu, Silica Restricting the Sulfur Volatilization of Nickel Sulfide for High-Performance Lithium-Ion Batteries , Adv. Energy Mater. 2019, 1901153.

[38] L. J. Zhang, X. Q. Hao, Y. P. Wang, Z. L. Jin, Q. X. Ma, Construction strategy of Mo-S@Mo-P heterojunction formed with in-situ phosphating Mo-S nanospheres toward efficient photocatalytic hydrogen production, https://doi.org/10.1016/j.cej.2019.123545.

[39] D. D. Liu, Z. L. Jin, Y. P. Bi, Charge transmission channel construction between a MOF and rGO by means of Co-Mo-S modification, Catal Sci Technol, 2017, 7, 4478-4488

[40] L. J. Zhang, X. Q. Hao, Y. B. Li, Z. L. Jin, Performance of WO_3/g-C_3N_4heterojunction composite boosting with NiS for photocatalytic hydrogen evolution, Appl. Surf. Sci, 2020, 499, 143862.

[41] C. J. Huang, C. Chen, M. W. Zhang, L. H. Lin, X. X. Ye, S. Lin, M. K. Antonietti, X. C. Wang, Carbon-doped BN nanosheets for metal-free photoredox catalysis, Nat. Commun, 2015, 6, 7698.

[42] K. L. He, J. Xie, M. L. Li, X. Li, In situ one-pot fabrication of g-C_3N_4 nanosheets/NiS cocatalyst heterojunction with intimate interfaces for efficient visible light photocatalytic H_2 generation, Appl. Surf. Sci, 2018, 430, 208-217.

[43] S. M. Lyth, Y. Nabae, S. Moriya, S. Kuroki, M. A. Kakimoto, J. I. Ozaki, S. Miyata, Carbon nitride as a nonprecious catalyst for electrochemical oxygen reduction, J. Phys. Chem. C, 2009, 113, 20148-20151.

[44] H. Yang, Z. L. Jin, D. D. Liu, K. Fan, G. R. Wang, Visible light harvesting and spatial charge separation over creative Ni/CdS/Co_3O_4 photocatalyst, J. Phys. Chem. C, 2018, 122, 10430-10441.

[45] X. Q. Hao, J. Zhou, Z. W. Cui, Y. C. Wang, W. Ying, Z. G. Zou, Zn-vacancy mediated electronhole separation in ZnS/g-C_3N_4 heterojunction for efficient visible-light photocatalytic hydrogen production, Appl. Catal. B: Environ, 2018, 229, 41-51.

[46] H. Yang, Z. L. Jin, G. R. Wang, D. D. Liu, K. Fan, Light-assisted synthesis MoSx as a noble metal free cocatalyst formed heterojunction CdS/Co_3O_4 photocatalyst for visible light harvesting and spatial charge separation, Dalton Trans, 2018,47, 6973-6985.

[47] L. J. Zhang, X. Q. Hao, Q. Y. Jian, Z. L. Jin, Ferrous oxalate dehydrate over CdS as Z-scheme photocatalytic hydrogen evolution, J Solid State Chem, 2019, 274, 286-294.

[48] H. Yang, Z. L. Jin, H. Y. Hu, Y. P. Bi, G. X. Lu, Ni-Mo-S nanoparticles modified graphitic $C_3N_4$for efficient hydrogen evolution, Appl. Surf. Sci, 2018, 427, 587-597.

[49] L. J. Zhang, Z. L. Jin, Y. P. Zhang, H. Y. Wang, Properties of iron vanadate over CdS nanorods for efficient photocatalytic hydrogen production, New J. Chem, 2019, 43, 3609-3618.

[50] G. X. Zhao, G. G. Liu, H. Pang, H. M. Liu, H. B. Zhang, K. Chang, X. U. Meng, X. J. Wang, J. H. Ye, Improved Photocatalytic H2 Evolution over G-Carbon Nitride with Enhanced In-Plane Ordering, Small 2016, 12, 6160-6166.

[51] R. C. Shen, J. Xie, X. Y. Lu, X. B. Chen, X. Li, Bi-functional Cu_3P Decorated g-C_3N_4Nanosheets as a Highly Active and Robust Visible-Light Photocatalyst for H_2 Production, ACS Sustainable Chem. Eng, 2018, 6, 3, 4026-4036.

[52] Y. K. Zhang, Z. L. Jin, Accelerated charge transfer via nickel tungstate modulated cadmium sulfide p-n heterojunction for photocatalytic hydrogen evolution, Catal. Sci. Technol, 2019, 9, 1944-1960.

[53] F. Guo, W. L. Shi, H. B. Wang, M. M. Han, H. Li, H. Huang, Y. Liu, Z. H. Kang, Facile fabrication of a CoO/g-C_3N_4 p-n heterojunction with enhanced photocatalytic activity and stability for tetracycline degradation under visible light, Catal. Sci. Technol. 2017, 7, 3325-3331.

[54] Y. Liu, G. R. Wang, Y. B. Li, Z. L. Jin, 2D/1D $Zn_{0.7}Cd_{0.3}S$ p-n heterogeneous junction enhanced with $NiWO_4$ for efficient photocatalytic hydrogen evolution, J Colloid Interf Sci, 2019, 554, 113-124.

Supplementary Information

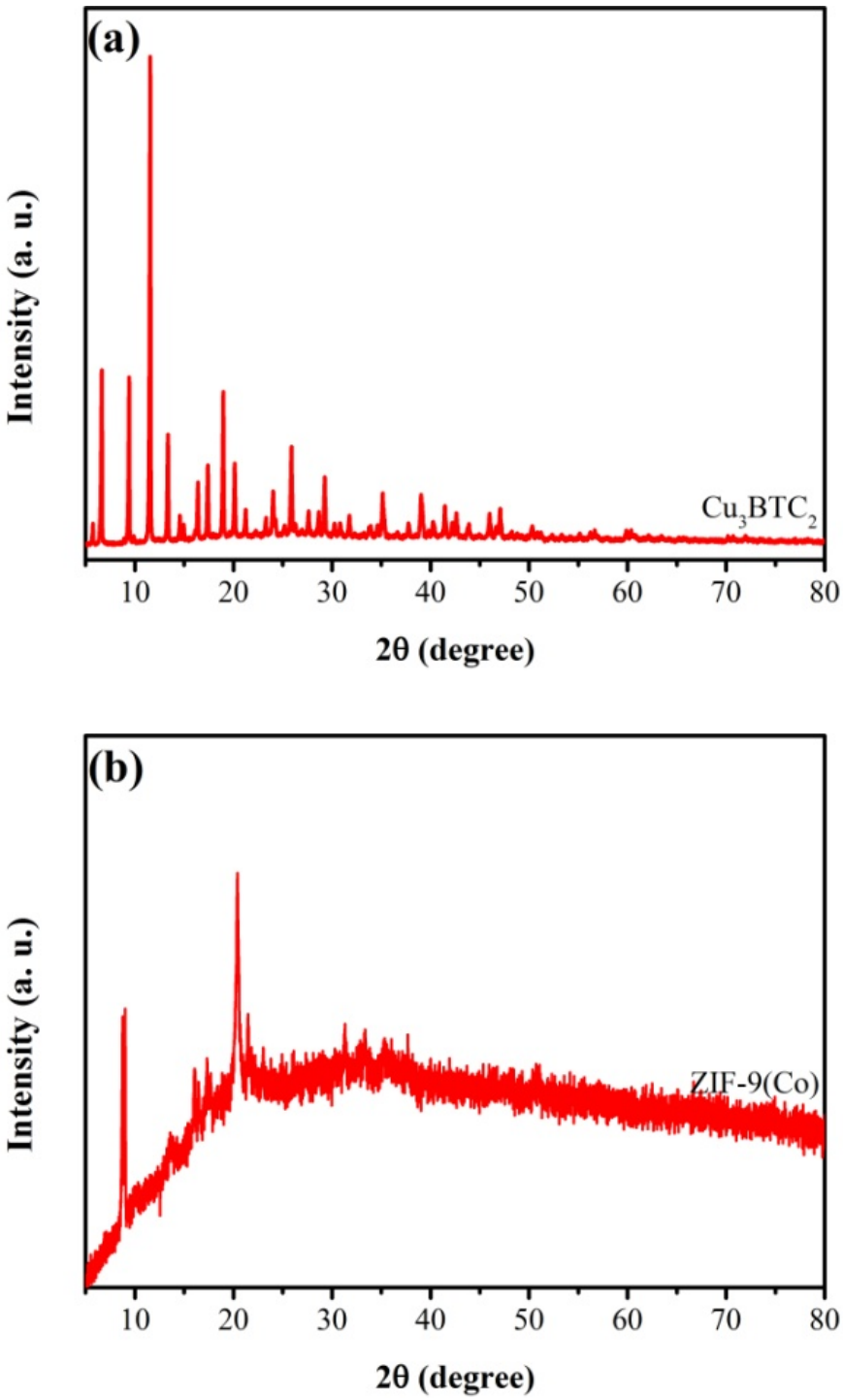

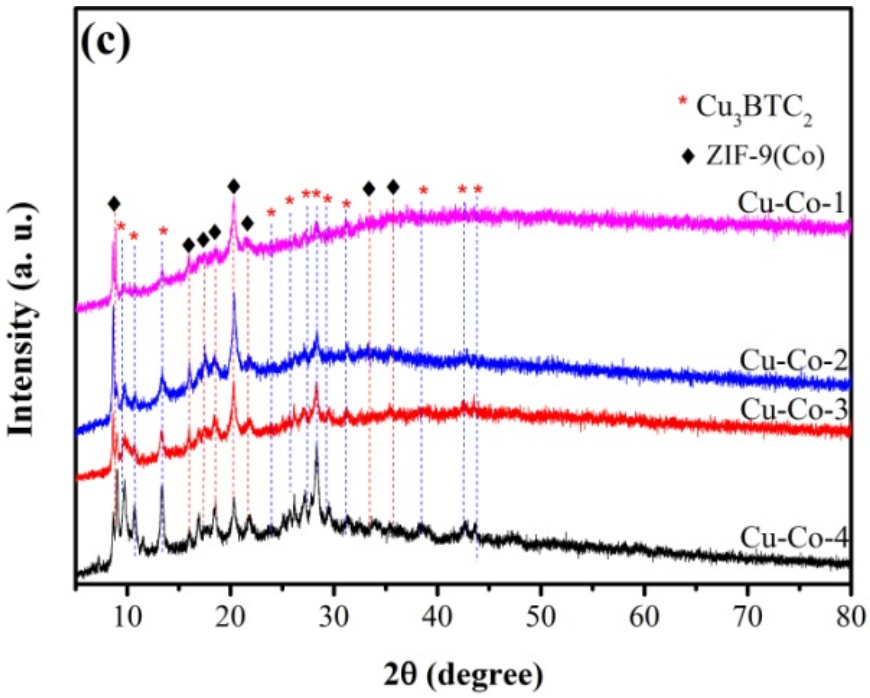

Figure S1. XRD patterns of Cu_3BTC_2 (a), ZIF-9(Co) (b); Cu-Co-x(x=1, 2, 3, 4.) (c).

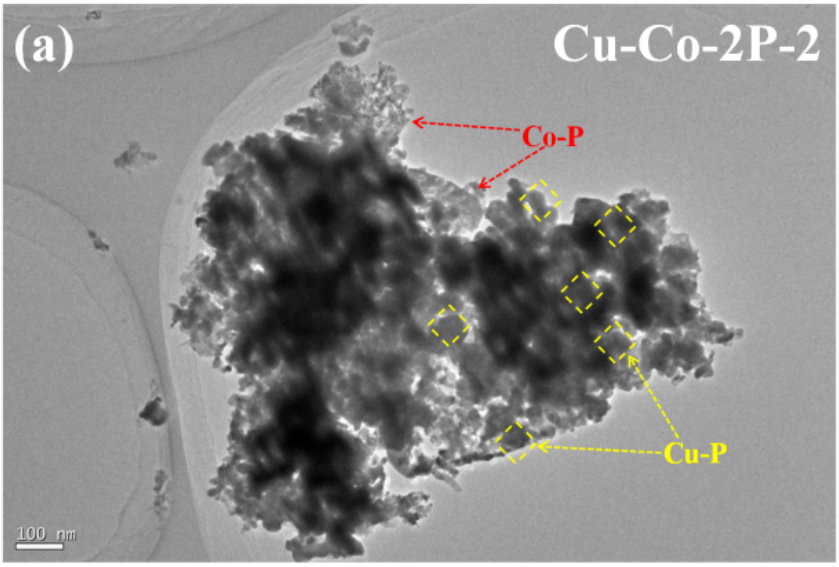

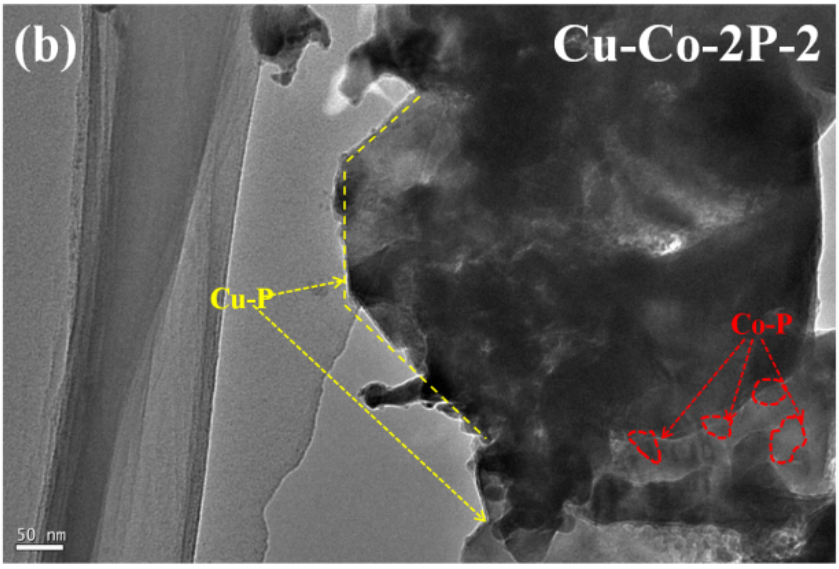

Figure S2. (a, b) TEM image of Cu-Co-2P-2.

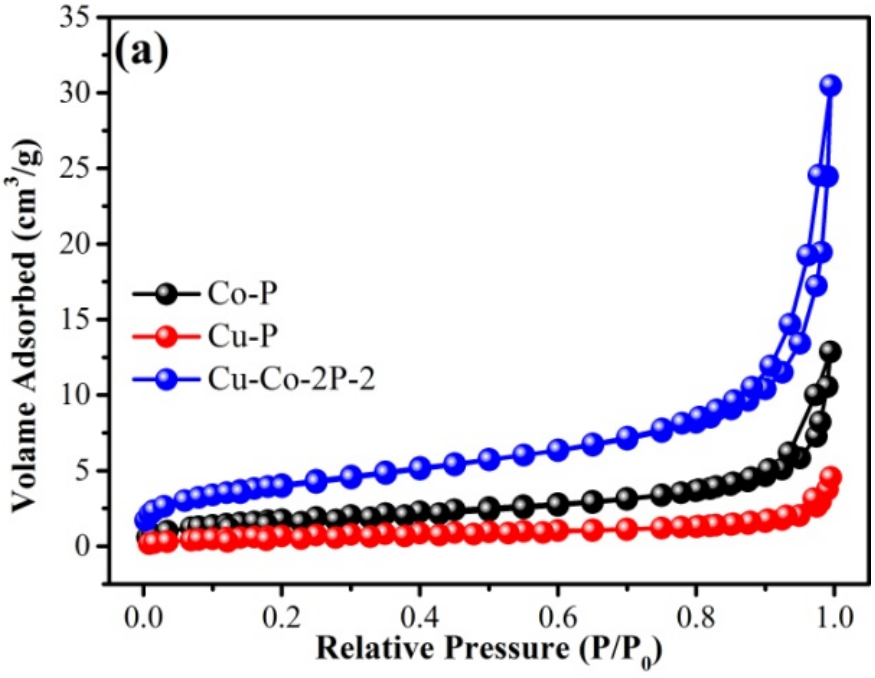

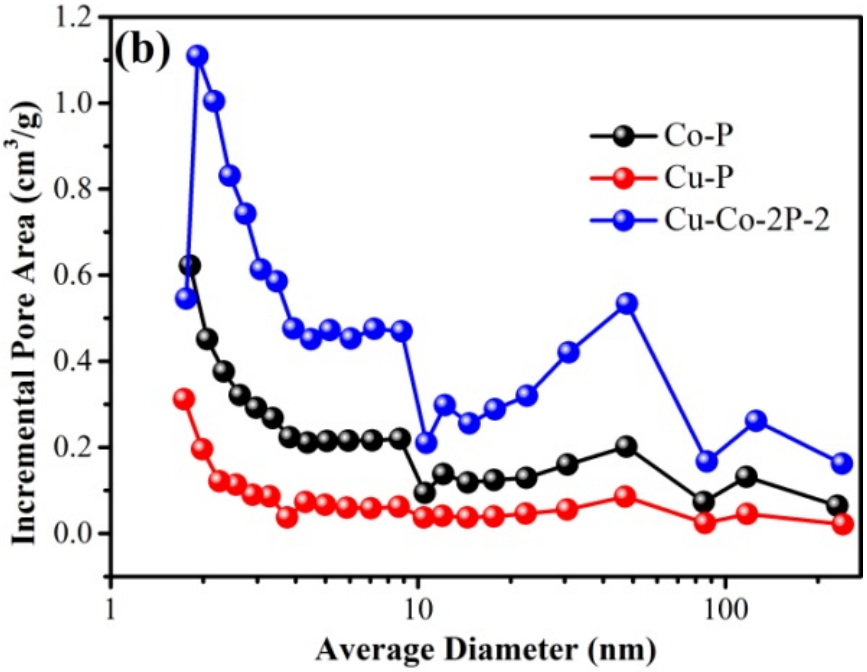

Figure S3. N_2 isothermal adsorption curves (a) and BJH adsorption mean pore size distribution of the sample of Co-P, Cu-P and Cu-Co-2P-2 (b).

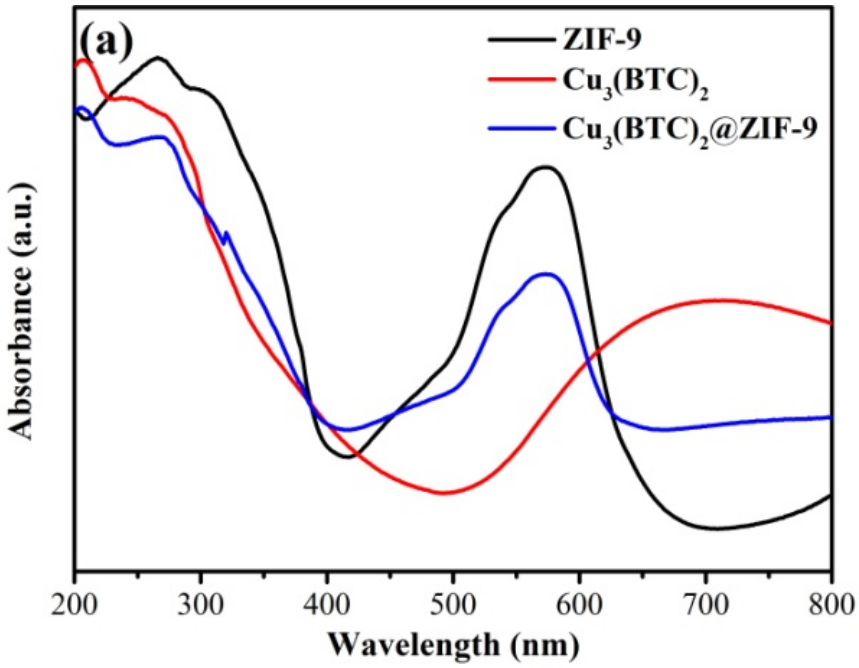

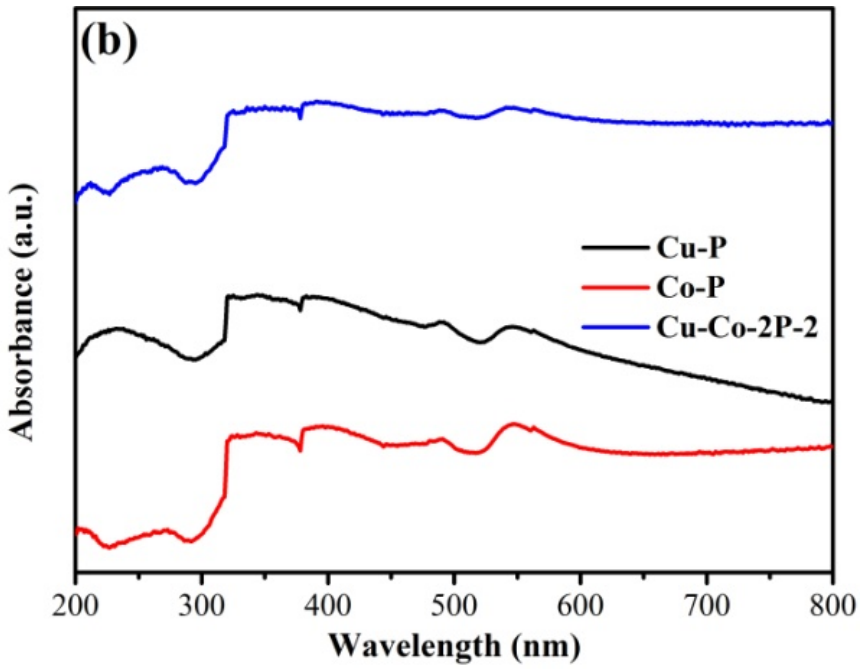

Figure S4. UV-vis DRS of ZIF-9, Cu-MOFs and Cu-MOFs@ZIF-9(a); Cu-P, Co-P and Cu-Co-2P-2 (b).

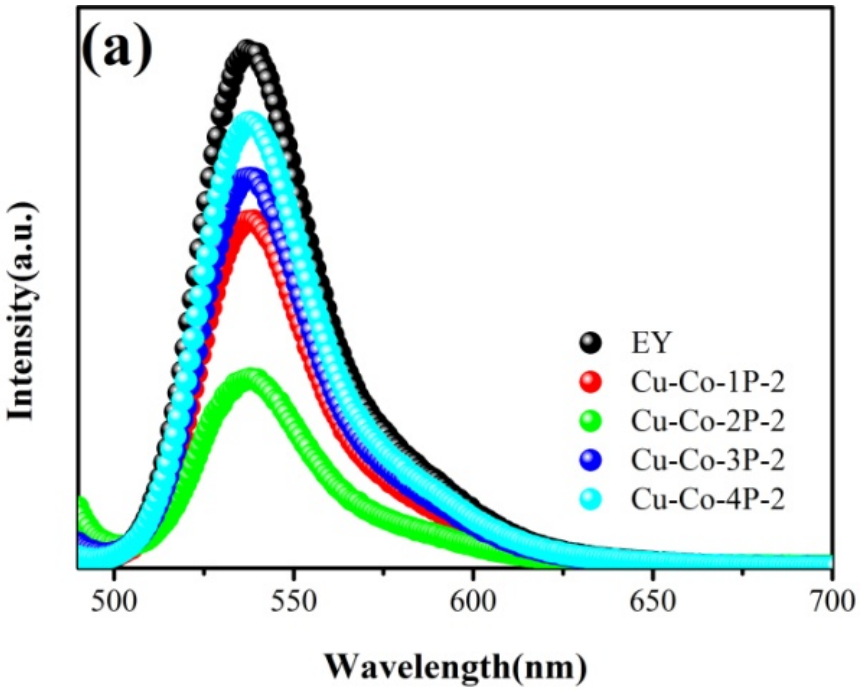

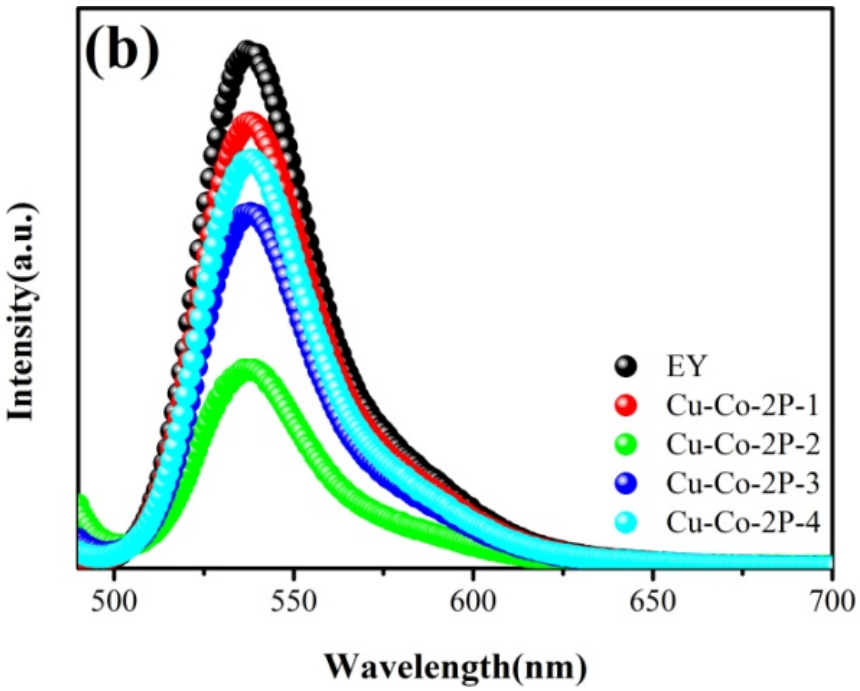

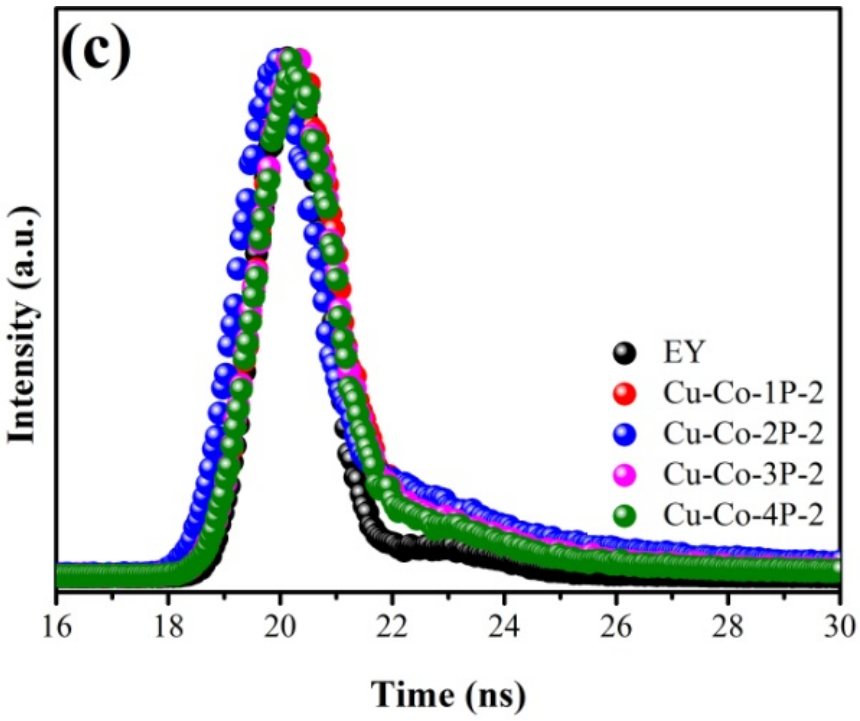

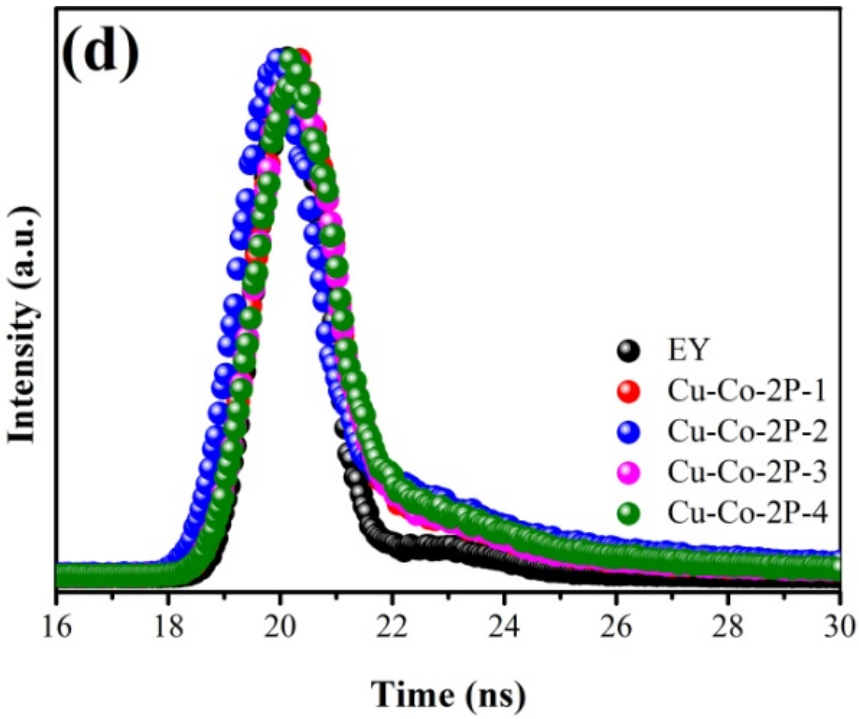

Figure S5. Steady-state fluorescence spectrum of the eosine sensitization system (a, b) and transient fluorescence spectrum(c, d).